Stationary Crossflow Vortices' Secondary Instability: Linear Stability Theory and Parabolized Stability Equations

Biagio Ambrosino*
Universidad Polit\'ecnica de Madrid, Plaza Cardenal Cisneros 3, E-28040 Madrid, Spain
Francesco Tocci,† Alexander Theiß,† and Stefan Hein†
German Aerospace Center, Department of High Speed Configurations, Institute of Aerodynamics and Flow Technology, 37073 Göttingen, Germany
and
Daniel Rodríguez‡
Universidad Polit\'ecnica de Madrid, Plaza Cardenal Cisneros 3, E-28040 Madrid, Spain

https://doi.org/10.2514/1.J064663

Three-dimensional laminar boundary layers over swept wings are susceptible to crossflow instabilities, manifesting as stationary and traveling crossflow vortices. The boundary layer distorted by these vortices is prone to the growth of secondary instabilities. Discrepancies between direct numerical simulation (DNS) and stability methodologies on the development of secondary perturbations of stationary crossflow vortices over swept wings have been reported in the literature. To shed light on the origin of these inconsistencies, a comparison of DNS and linear stability theory is provided here. Secondary disturbances of finite-amplitude stationary crossflow vortices are analyzed for two frequencies: $f = 900$ Hz (Type III secondary instability) and $f = 2200$ Hz (Type I secondary instability). Results from linear stability theory (LST-2D) and linear parabolized stability equations (PSE-3D) formulated in a suitable nonorthogonal coordinate system correlate well with DNS data in terms of perturbation shape and location relative to the stationary crossflow vortices. Employing a nonorthogonal coordinate system is crucial for PSE-3D to fulfill slow variation along the streamwise direction and spanwise periodicity, whereas LST-2D, assuming parallel flow, can also use periodic boundary conditions in a vortex-aligned orthogonal coordinate system. However, the LST-2D results underestimate the integrated growth rate, whereas the PSE-3D computations closely match the DNS, highlighting the importance of including streamwise gradients and upstream history in the instability computations.

Nomenclature

$c_{x_\perp}$	=	chord length in the $x_\perp$ direction
E	=	total kinetic energy
f	=	frequency of the unsteady perturbation
J	=	number of subdomains Ω_i
M	=	Mach number
N	=	number of points in the plane yz
n	=	n-factor, integrated growth rate
P^*	=	nondimensional power spectral density of the chordwise velocity fluctuations
p_∞	=	freestream pressure
q	=	degree of the piecewise polynomial interpolant in the FD-q discretization scheme
$\boldsymbol{q}$	=	total flow vector in the xyz coordinate system
$\bar{\boldsymbol{q}}$	=	base flow vector in the xyz coordinate system
$\tilde{\boldsymbol{q}}$	=	unsteady perturbation vector in the xyz coordinate system
$\hat{\boldsymbol{q}}$	=	vector of amplitude functions
$Re_{c_{x_\perp}}$	=	Reynolds number based on $c_{x_\perp}$
Tu	=	freestream turbulence intensity
t	=	time
u_∞	=	freestream velocity
u, v, w	=	contravariant velocity components in the xyz coordinate system
u_c, v_c, w_c	=	velocity components in the $x_\perp y z_\parallel$ coordinate system
u_g, v_g, w_g	=	velocity components in the $x_g y_g z_\parallel$ coordinate system
x, y, z	=	nonorthogonal coordinate system
x', y, z'	=	orthogonal body-fitted coordinate system aligned with the crossflow vortex axis
$x_g, y_g, z_\parallel$	=	cartesian coordinate system
$x_\perp, y, z_\parallel$	=	curvilinear body-fitted coordinate system
α	=	wavenumber of the disturbance in the x direction
β_0	=	wavenumber of the disturbance in the z direction
δ_0	=	displacement thickness at the inlet boundary of the DNS domain
ε	=	small number, $\varepsilon \ll 1$
θ	=	angle between x and $x_\perp$
$\theta_{\min}$	=	$\theta \to \partial u/\partial x|^*_{\S,\min}$
λ_0	=	wavelength in the z direction
λ_2	=	lambda-2 criterion
μ	=	dynamic viscosity
ρ	=	density
σ	=	spatial growth rate
ω	=	circular frequency

Subscripts and superscripts

$(\cdot)_i$	=	imaginary part
$(\cdot)_r$	=	real part
$(\cdot)^\dagger$	=	complex conjugate
$(\cdot)\|^*$	=	nondimensional quantity
$(\cdot)\|_\S$	=	root mean square value

I. Introduction

IN RECENT years, the rising cost of fossil fuels and heightened environmental concerns have renewed interest in laminar wing technology. The aim is to reduce the skin-friction drag, which

Presented as Paper 2024-4488 at the AIAA Aviation 2024 Forum, Las Vegas, NV, July 29–August 2, 2024; received 24 July 2024; accepted for publication 9 December 2024; published online Open Access 11 March 2025.

*Research Scientist, Department of High Speed Configurations, DLR Göttingen; biagio.ambrosino@dlr.de (Corresponding Author).
†Research Scientist, Department of High Speed Configurations, DLR Göttingen.
‡Professor, Department of Applied Mathematics in Aerospace Engineering.

accounts for approximately one-half of the total drag for civil airliners, by delaying laminar to turbulent transition [1]. The transition from laminar to turbulent flow in three-dimensional (3-D) boundary layers over swept wings is a complex phenomenon that significantly impacts the aerodynamic performance of aircraft. The need to control the laminar–turbulent transition process in swept-wing flows motivates the research on 3-D boundary layers.

Subsonic two-dimensional boundary-layer transition is often characterized by Tollmien–Schlichting (TS) waves. On the other hand, 3-D boundary layers are characterized by a different transition process. A swept-wing boundary layer is susceptible to different kinds of instabilities such as attachment-line instability [2,3], TS waves [4], Görtler vortices [5], and crossflow instabilities (CFI) [6,7]. The latter remains one of the most critical instabilities because the lamina–turbulent transition process in swept-wing boundary layers is often initiated by either stationary or traveling CFI [8]. The favorable pressure gradient in the leading-edge region of swept wings in combination with a sweep angle results in a flowfield that is characterized by a crossflow velocity component in the direction orthogonal to the inviscid streamline [9]. This velocity component is zero, both at the wall and at the edge of the boundary layer. It has at least one inflection point and is susceptible to the onset of an inviscid instability, commonly known as crossflow instability.

Experiments by Bippes at DLR [10] and numerical simulations by Schrader [11] have shown that stationary crossflow vortices, often excited by surface roughness, are the predominant crossflow instabilities in low-turbulence environments, whereas high-turbulence environments favor the development of traveling crossflow instabilities. This work focuses on boundary layers dominated by the development of stationary crossflow vortices, which is the scenario typically encountered in free-flight conditions [9]. These vortices redistribute momentum across the boundary layer, leading to a distortion of the otherwise spanwise invariant boundary layer. In particular, low-momentum fluid close to the wall is brought upward, whereas at other spanwise locations high-momentum fluid is brought toward the wall. This distortion gives rise to pronounced shear layers, rendering the boundary layer susceptible to the growth of secondary instabilities that finally trigger the laminar breakdown [12–14].

The literature identifies several families of secondary instabilities classified based on their location relative to the crossflow vortex. A sketch of the typical distorted boundary layer represented by chordwise velocity component isolines is provided in Fig. 1. Additionally, the typical onset locations of the different types of secondary instabilities are portrayed. The Type I and Type II instabilities, as designated by Koch et al. [15], were originally identified as z-mode and y-mode by Malik et al. [16], who discovered the association of the different types of secondary instabilities with different shear directions. This correlation was found by Malik et al. by computing and comparing all six nonzero shear production terms in the energy budget equation [16]. Furthermore, they were found by Koch et al. employing a two-dimensional eigenvalue approach to identify the secondary disturbances of stationary crossflow vortices. The first family of secondary instabilities, that is, Type I, was associated with the spanwise shear and is located on the shoulder of the stationary crossflow vortex. On the other hand, Type II is associated with the surface-normal gradient and resides on top of the stationary crossflow vortex. Högberg and Henningson [17] and Koch et al. [15] identified another instability mechanism, defined as Type III, which prevails at lower frequencies than Type I and Type II [15,18]. This low-frequency mode is dominant in a region close to the wall and it is related to the primary traveling crossflow instability modulated by the action of the stationary crossflow vortices. The high-frequency modes, that is, Type I and Type II, appear farther downstream than the low-frequency Type III mode. However, they exhibit a rapid and significant amplification over a relatively short streamwise extent, often exceeding the Type III in amplitude. In low-turbulence environments, these high-frequency modes typically trigger the transition from laminar to turbulent flow [15].

The evolution of secondary perturbations of crossflow vortices has been studied with different numerical approaches, revealing significant discrepancies, particularly when linear stability methods were compared to direct numerical simulation (DNS). Högberg and Henningson [17] conducted both linear eigenvalue analysis and spatial DNS to study the growth of disturbances in a Falkner–Skan–Cooke boundary layer. They found that the growth rates of small-amplitude disturbances obtained from the DNS calculations showed differences compared to the one obtained with the linear eigenvalue computations, indicating the presence of nonparallel effects. Koch et al. [15] computed the nonlinear equilibrium solution for the flow in the DLR swept-plate transition experiment [10]. This solution is then used as a base state for a Floquet analysis, formulated in an orthogonal coordinate system aligned with the vortex axis, of the secondary instabilities of the saturated vortices. Their numerical computations resembled the experimental results available at that time, both in terms of frequency range and eigenfunction shape. Bonfigli and Kloker [19] carried out a detailed comparison between DNS and secondary linear stability theory (SLST) for the 3-D crossflow-dominated base flow of the DLR-Göttingen experiment [10]. However, significant deviations in the amplification rates were found, with the SLST results being strongly dependent on the representation of the primary state, that is, the base flow. Highlighting the lack of a unique approach to define the base flow for SLST, they analyzed the effects of three different extraction procedures, showing that in all cases the SLST underestimated the amplification rate obtained from the DNS. Li and Choudhari [20] used a planar (two-dimensional) eigenvalue analysis methodology, that is, LST-2D, to study the spatial instabilities in both subsonic and supersonic shear flows with two inhomogeneous directions. Their methodology employed a nonorthogonal coordinate system and addressed the base flow extraction ambiguity by using planes parallel to the leading edge, which adhered to spanwise periodicity, and aligning the out-of-plane direction with the least variation of the distorted base flow. They analyzed the modification of the traveling crossflow modes and the destabilization of high-frequency secondary instabilities for finite-amplitude stationary crossflow vortices of a specified spanwise wavelength and varying initial amplitudes. They found that the onset of the secondary instability moved upstream as the initial amplitude of the stationary crossflow vortex was increased. Additionally, this resulted in a weak stabilization of the initially dominant traveling modes, which had been noted by Fischer and Dallmann [12] already. Fischer and Dallmann used a simplified approach in which the shape of the finite-amplitude stationary crossflow vortices was approximated by linear eigenfunctions. Xu et al. [21] employed the Floquet theory to study the secondary instabilities in an $M = 6$ swept-wing boundary-layer flow. They observed Type I and Type II secondary instabilities in a similar manner as in subsonic swept-wing flows. Moreover, they identified a new type of secondary instability amplified at the trough of the stationary crossflow vortex. This perturbation mainly extracts its energy from the wall-normal shear as the Type II secondary instability. Furthermore, Groskopf and Kloker [22] studied the influence of a 3-D skewed roughness element in a high-speed boundary layer. The oblique element induces a crossflow-vortex-like velocity distribution compared to the corresponding symmetric roughness element. The results displayed an overall good agreement between the DNS and the LST-2D results. Furthermore, they analyzed the sensitivity of the instability computations to different base flow representations, as applied by Bonfigli and Kloker [19]. They found that the base flow representation has a very small influence on the stability results, most likely due to lack of strong gradients in the direction orthogonal to the discretization plane, that is, chordwise direction. Groot et al. [23] employed two-dimensional linear stability theory (LST-2D), formulated in an orthogonal vortex-aligned coordinate system, to study an experimentally measured base flow, investigating in detail the role of the Type I and Type II secondary instabilities. Furthermore, Groot et al. [24] employed an LST-2D approach, formulated in an orthogonal coordinate system with the out-of-plane direction pointing in the chordwise direction, to study the effect of a supercritical forward-facing step on finite-amplitude stationary crossflow vortices. The base flow utilized for the stability analysis was measured by a high-resolution, stereographic particle image velocimetry. Several families of unstable modes, supported

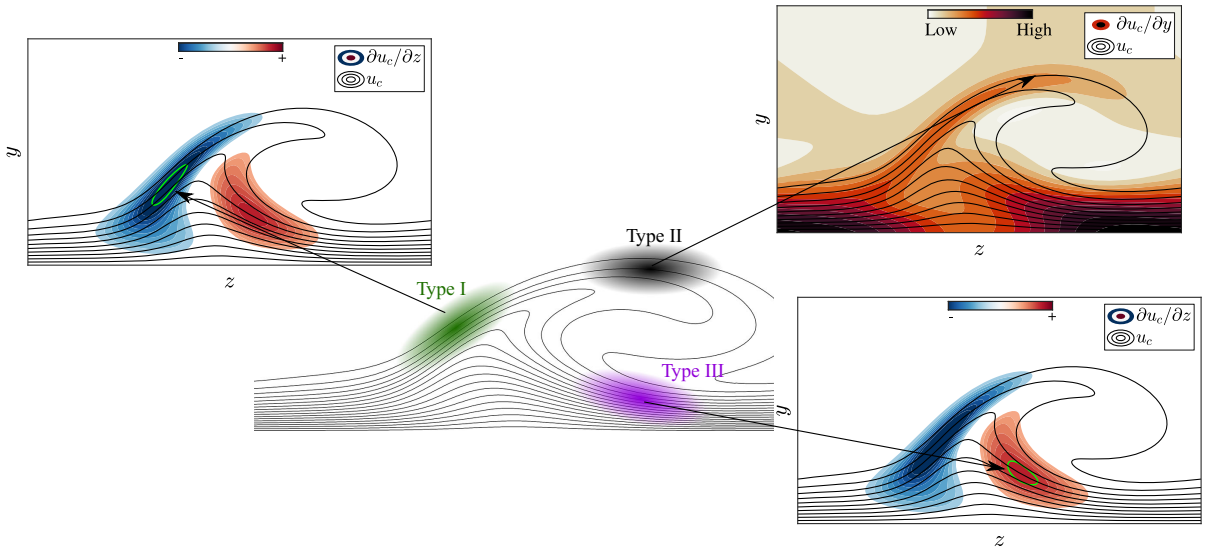

Fig. 1 Sketch of the distorted boundary layer due to the action of the stationary crossflow vortices. Color-shaded areas denote the locations of various secondary instabilities of crossflow vortices: Type I in green, Type II in black, and Type III in purple.

by the flowfield, were found downstream of the surface irregularity. Comparing the latter with the measured perturbation data in the form of spectral proper orthogonal decomposition modes revealed several differences. Groot et al. analyzed the same base flow but with a different formulation of the stability equations in [25]. They employed the approach proposed by Li and Choudhari [20] to formulate the stability equations in a nonorthogonal coordinate system, which resulted in larger growth rates and a significant improvement in the comparison of the eigenfunctions with the experimental results. Li et al. [26] and Choudhari et al. [27] employed a linear plane-marching parabolized stability equation (PSE-3D) to study the evolution of secondary instabilities over a yawed cone in a hypersonic flow regime. They reported a good agreement of the stability results in terms of amplitude function shape and integrated growth rate with the DNS results. Casacuberta et al. [28] compared the secondary instability modes computed with LST-2D with those obtained from an unsteady DNS. The LST-2D equations were derived in a nonorthogonal coordinate system following the approach of Li and Choudhari [20]. They have reported an overall good agreement in terms of eigenfunctions and integrated growth rates for a Type I and Type III secondary instability, even though major discrepancies between the DNS and stability analysis results arise in the upper portion of the crossflow vortex when moving downstream along the streamwise direction.

The current study is driven by the uncertainty in predicting secondary instabilities of stationary crossflow vortices over incompressible swept wings using a linear stability tool, and goes beyond established approaches by employing not only LST-2D but also the plane-marching parabolized stability equations, that is, PSE-3D, in a nonorthogonal coordinate system. The accuracy of the instability computations is proved by comparing them with DNS results. The paper is organized as follows: Sec. II presents the flow conditions and the different coordinate systems, Sec. III.A outlines the numerical methodology employed in the DNS, and Sec. III.B analyzes the main characteristics of the base flow with the aim of selecting the most suitable coordinate system to perform the stability analysis. Sec. III.B also discusses the setup for the LST-2D and PSE-3D stability formulations. Sec. IV compares the results of the stability methods with the DNS data. Finally, Sec. V provides the conclusions and summarizes the findings of this study.

II. Setup and Flow Conditions

The flow configuration is designed to numerically replicate the experiments performed by Rius–Vidales et al. [29] in the Low Turbulence Tunnel (LTT) at the Delft University of Technology. The setup consists of a 45-deg swept-wing model with a chord length normal to the leading edge of $c_{x_\perp} = 0.9$ m. The model is oriented vertically in the test section of the wind tunnel at an angle of attack AoA = 3 deg. The airfoil profile is a modified NACA 66018, as described by Serpieri et al. [30], which promotes the growth of CFI under mild angles of attack by maintaining a favorable pressure gradient up to $x/c_{x_\perp} \approx 0.65$. The design avoids concave surfaces and features a small leading-edge radius, about 1% of the chord, to prevent the amplification of Görtler vortices and attachment-line instabilities, as discussed by Bippes [10]. At reference experimental conditions, the freestream turbulence intensity, defined as $Tu = (1/u_\infty)\sqrt{(u'^2 + v'^2)/2}$, is less than 0.03%, ensuring that stationary crossflow vortices dominate the laminar-turbulent transition [10,31]. Discrete roughness elements (DRE), introduced near the leading edge, trigger a CFI mode with a spanwise wavelength of $\lambda_0 = 7.5$ mm and a corresponding wavenumber of $\beta_0 = 837.758\,\mathrm{m}^{-1}$. To closely mimic the near-field flow of the airfoil, the far-field flow parameters were set as follows in the DNS [32]: freestream velocity $u_\infty = 27.542\,\mathrm{m\,s}^{-1}$ (measured just upstream of the model using a pitot-static tube), freestream pressure $p_\infty = 9.941 \times 10^4$ Pa, density $\rho = 1.2069\,\mathrm{kg\,m}^{-3}$, and dynamic viscosity $\mu = 1.7829 \times 10^{-5}\,\mathrm{kg\,m}^{-1}\mathrm{s}^{-1}$. These parameters result in a chord Reynolds number of $Re_{c_{x_\perp}} = 2.37 \times 10^6$. The boundary-layer displacement thickness at the inlet, $\delta_0 = 5.25 \times 10^{-4}$ m, is the characteristic quantity used to nondimensionalize the spatial coordinates.

A. Coordinate Systems

Different coordinate systems have been used for computations and visualization purposes. In the DNS, a Cartesian coordinate system (x_g, y_g, $z_\parallel$) is employed, where $z_\parallel$ is the spanwise direction and it is parallel to the leading edge of the wing, x_g is perpendicular to the leading edge, and y_g is normal to those two directions, cf. Fig. 2. The corresponding velocity components are (u_g, v_g, w_g). Some results are presented in the curvilinear coordinate system ($x_\perp$, y, $z_\parallel$), portrayed in Fig. 2, with the corresponding velocity components (u_c, v_c, w_c). It has the same origin (the origin is shifted for an improved visualization in the plot) and the same spanwise coordinate $z_\parallel$, with $x_\perp$ being perpendicular to the leading edge and tangent to the wing surface, whereas y is normal to the surface of the wing. In the following, the $x_\perp$ direction will be also referred to as chordwise. The stability analysis results are computed in a nonorthogonal coordinate system (x, y, z), which is discussed more in detail in Sec. III.B.1. The corresponding contravariant velocity components are (u, v, w).

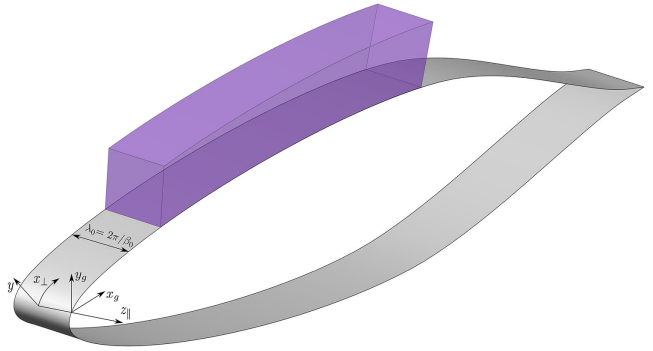

Fig. 2 Overview of the geometry alongside the Cartesian and the orthogonal curvilinear coordinate systems. The computational domain employed for the 3-D DNS is highlighted in purple.

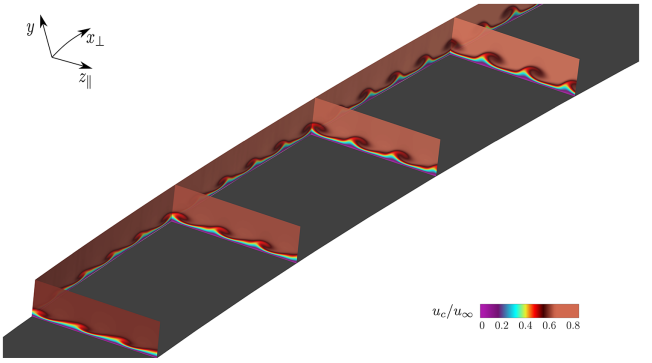

Fig. 3 Pseudocolor of the normalized instantaneous $x_\perp$-velocity component (u_c/u_∞) extracted from the steady DNS at different $yz_\parallel$ and $x_\perp y$ planes.

III. Numerical Methods

This section introduces the different numerical methodologies used in this work. First, a brief overview of the DNS is given. The numerical simulations, conducted as part of another work [32], not only provide the steady base flow for the instability analysis, but also provide the unsteady results that serve as benchmarks for the secondary instability results from LST-2D and PSE-3D. The second part of the section introduces these two linear instability analysis approaches, emphasizing the selection of the optimal coordinate system to solve the corresponding stability equations.

A. DNS

DNS are performed with the spectral element method (SEM) code Nek5000 [33]. The SEM decomposes the physical domain into spectral elements, where the flowfield solution is given by a sum of Lagrange interpolants defined by an orthogonal basis of Legendre polynomials within each element.

1. *Steady DNS*

Due to the high computational cost of 3-D DNS, these computations are conducted on a relatively small domain, requiring adequate boundary conditions. These conditions are derived in a two-step process. First, RANS equations are employed to perform an infinite-swept wing (two-and-a-half dimensional or 2.5-D) computation on a section of the wind tunnel that includes the entire airfoil shape and the tunnel walls. The flowfield resulting from this calculation sets the far-field conditions for a subsequent 2.5D DNS, which provides an accurate spanwise-invariant steady-state flowfield in an intermediate-sized domain. The data derived from this step provides the boundary conditions for the 3-D DNS. The computational domain in the spanwise direction is limited to a single wavelength λ_0, with periodic boundary conditions applied along this spanwise axis, that is, $z_\parallel$. Figure 2 illustrates the swept airfoil and the reduced domain adopted for the 3-D DNS highlighted in purple. The inflow boundary of the 3-D DNS domain is placed at $x_g/c_{x_\perp} \approx 0.1$. The receptivity stage, namely the generation of the crossflow vortices by the DRE in the experiments, is not considered in the DNS performed here. Instead, the stationary crossflow vortices are imposed as a boundary condition on the inflow boundary of the domain, superposed to the spanwise invariant base flow from the 2.5-D DNS. Their shape and amplitude were determined using nonlinear PSE [34]. When only steady crossflow vortices are introduced at the inflow of the 3-D DNS, the simulations do not exhibit a transition to turbulence due to the minimal numerical noise. The resulting steady distorted flowfield is shown in Fig. 3. In the following sections, the latter will be referred to as the base flow.

2. *Unsteady DNS*

To emulate the unsteadiness caused by the nonzero freestream disturbance environment of the LTT wind tunnel in the DNS, unsteady perturbations are artificially induced inside the boundary layer just downstream of the inflow boundary by applying a randomly pulsed volume force. This perturbation strategy is similar to the "trip forcing" method delineated by [35]. It is implemented in the momentum equation as a force component normal to the wall and introduces perturbations within a specific range of spanwise wavenumbers ($\beta = m\beta_0$ with $m = 1, 2, \ldots, 16$) and 400 discrete frequencies equally distributed in the interval $f = 0 - 10$ kHz. The noise amplitude is calibrated to ensure that the location of the transition from laminar to turbulent flow in the simulations correlates closely with the experimental observations. In the postprocessing phase, the velocity field is decomposed through a Fourier transformation in time, isolating a single mode for comparison with the results of the instability analysis.

B. Instability Analysis

1. *Choice of the Coordinate System*

The base flow used in the stability analysis to study the evolution of the secondary perturbations is shown in Fig. 3. It can be seen that the boundary layer is strongly distorted due to the action of the stationary crossflow vortices. As a consequence, it displays a wavy pattern in the chordwise and spanwise directions. The most suitable coordinate system for solving the stability equations is chosen based on the principal characteristics of the base flow. This choice is driven by the need to comply with the LST-2D and PSE-3D assumptions (see Sec. III.B.2), which require zero or slow variation along the x direction, respectively. An overview of different potential coordinate systems is shown in Fig. 4. In addition, the trace of the stationary crossflow vortex projected onto the surface $x_\perp z_\parallel$ is indicated in the plot by the gray-shaded area. The solid orange line denotes the axis of the crossflow vortex and the blue dashed line indicates the inviscid streamline. A primary consideration in selecting the appropriate coordinate system is the periodicity of the base flow in the direction parallel to the leading edge, that is, $z_\parallel$. An orthogonal system ($x_\perp$, y, $z_\parallel$), as shown in Fig. 4a, could be contemplated to align with this periodic characteristic. However, despite fulfilling the periodicity of the base flow along the $z_\parallel$ direction, the gradient of the base flow quantities in the orthogonal out-of-plane direction, that is, $x_\perp$, may be large due to the action of the finite-amplitude stationary crossflow vortex, rendering the choice of this coordinate system incompatible with the assumptions of both LST-2D and PSE-3D. Consequently, this choice is inappropriate and must be discarded. To satisfy the assumption of the stability theory, a direction along which the distorted base flow quantities vary the least [28] has to be employed. An orthogonal coordinate system, that is, (x', y, z') as shown in Fig. 4b, with x' direction aligned along this direction of minimal gradient and z' direction orthogonal to the x' direction, would initially seem appropriate. However, this coordinate system would not allow one to apply the periodic boundary condition in the z' direction in the context of the PSE-3D. Thus, to simultaneously satisfy the criteria of spanwise periodicity and slow variation along the x direction, a nonorthogonal coordinate system as shown in Fig. 4c is chosen.

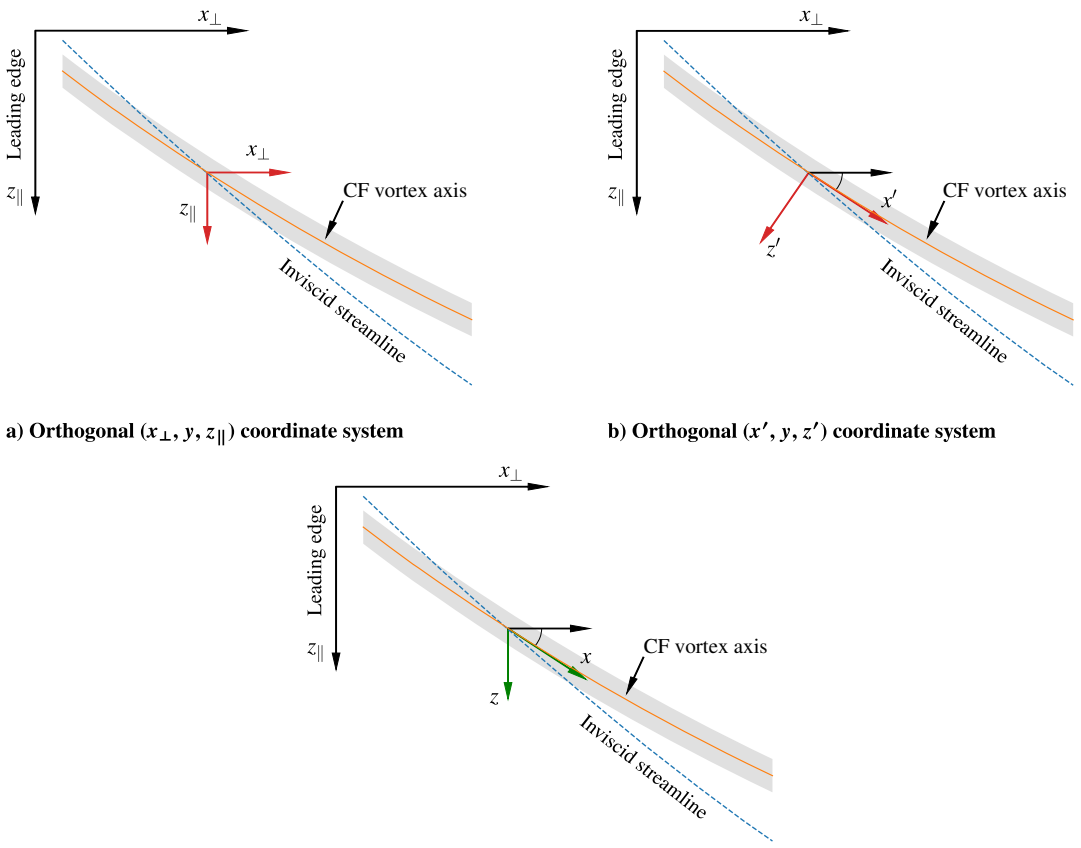

a) Orthogonal $(x_\perp, y, z_\parallel)$ coordinate system

b) Orthogonal (x', y, z') coordinate system

c) Nonorthogonal (x, y, z) coordinate system

Fig. 4 Sketch of different possible coordinate system choices for the formulation of the stability problem.

In this coordinate system, the x direction is aligned with the direction of least variation of the base flow derivatives at each x position and will be referred to as streamwise, while the z direction is parallel to the leading edge and its origin is shifted with respect to the $z_\parallel$ coordinate, being zero along the x axis, while $z_\parallel$ equals zero along the $x_\perp$ axis [see Appendix, Eq. (12)]. The component of vectors in this coordinate system can be represented by two different formulations named covariant and contravariant. As underlined in the Appendix, the latter is adopted in the current implementation and the (u, v, w) are the contravariant components of the velocity vector in the nonorthogonal coordinate system. The angle θ represents the deviation of the x coordinate from the chordwise direction and is determined in a similar manner as in [28]. The out-of-plane derivatives $\partial u/\partial x$, $\partial v/\partial x$, and $\partial w/\partial x$ are evaluated, and the root mean square (rms) of these derivatives is computed at all x positions over each yz plane. The rms of the derivatives is denoted by $\partial(\cdot)/\partial(\cdot)|_{\S}$ and is evaluated as $(\cdot)_{\S} = \sqrt{1/N \sum_{j=1}^{N} |(\cdot)_j|^2}$, where N is the number of points in the plane yz. Then, the direction along which the derivatives are computed, and thus the angle θ, is varied until the minimum rms value of these derivatives is obtained for each component separately. Figure 5 elucidates this process: on the left a sketch of the base flow at two subsequent $x_\perp$ positions is shown, indicating both the $x_\perp$ and x directions. On the right, the normalized

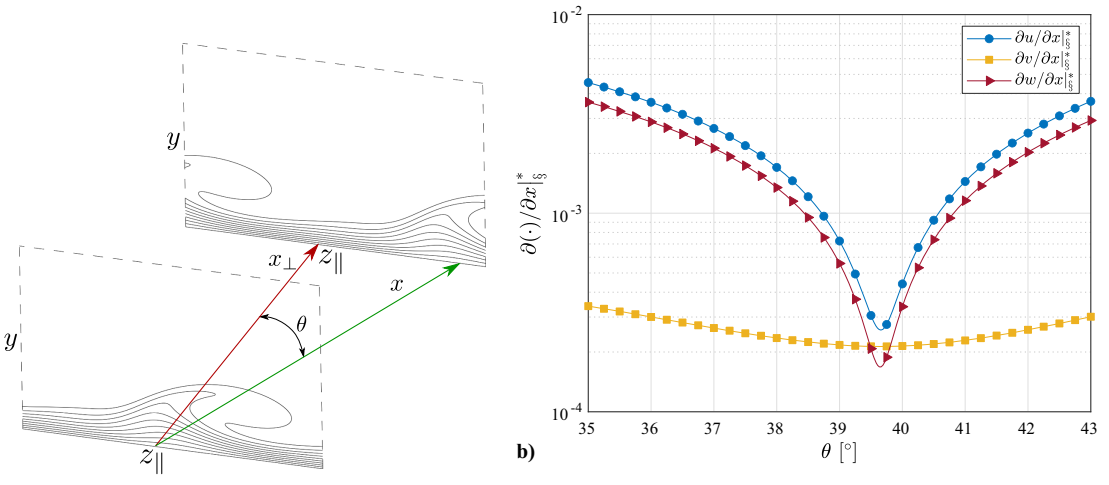

a)

b)

Fig. 5 a) Sketch of the distorted base flow and the out-of-plane directions x and $x_\perp$, and b) variation of the normalized rms of the out-of-plane velocity gradients as function of the angle θ at the station $x_\perp/\delta_0 = 650$.

out-of-plane velocity gradients are shown as a function of the angle θ for the station $x_\perp/\delta_0 = 650$. The normalization of the derivatives is conducted as follows:

$$\left.\frac{\partial u}{\partial x}\right|^* = \frac{\partial u}{\partial x}\frac{\delta_0}{u_\infty}, \quad \left.\frac{\partial v}{\partial x}\right|^* = \frac{\partial v}{\partial x}\frac{\delta_0}{u_\infty}, \quad \left.\frac{\partial w}{\partial x}\right|^* = \frac{\partial w}{\partial x}\frac{\delta_0}{u_\infty} \tag{1}$$

It is worth noting that even a marginal deviation in the angle θ from its optimal value, for which the rms of the derivatives is minimized, causes a significant change in the out-of-plane gradient of both the streamwise and spanwise velocity components. In particular, Fig. 5 shows that a change of about 4-deg can increase the rms of the derivatives by nearly two orders of magnitude, which, as Sec. IV will elucidate, significantly affects the instability results.

Figure 6 shows the angle for which the three rms of the derivatives have a minimum as a function of the chordwise coordinate $x_\perp$. It is interesting to observe that those curves almost coincide, deviating only by a few degrees from the angle of the external inviscid streamline. Furthermore, it can be noted that the angles for which the three rms of the derivatives have a minimum closely align with the angle of the crossflow vortex axis. This confirms that the direction of least variation is very close to the one of the crossflow vortex axis. The latter was evaluated by adopting the vortex tracking procedure employed in [36] and is described more in detail in [37]. In addition, Fig. 7 shows the rms of the velocity derivatives as a function of the chordwise direction. Figure 7a illustrates these gradients in the orthogonal $(x_\perp, y, z_\parallel)$ coordinate system, whereas Fig. 7b depicts them in the nonorthogonal (x, y, z) system. It can be noted that the out-of-plane derivatives in the orthogonal system are of the same order of magnitude as the spanwise derivatives and only one order of magnitude smaller than the wall-normal shear. When analyzing the data in the nonorthogonal coordinate system, where the out-of-plane axis is aligned along the direction θ that minimizes the $\partial u/\partial x|^*_\S$, a substantial reduction is observed in the out-of-plane gradients of both the spanwise and streamwise velocity components. This direction will be referred to as $\theta_{\min}$. These gradients decrease by about two orders of magnitude, that is, from 10^{-2} to 10^{-4}. It can be noted that, as expected, the wall-normal velocity derivatives do not change when moving from the orthogonal to the nonorthogonal coordinate system.

Moreover, Fig. 8 illustrates the out-of-plane derivative of u_c and u in both coordinate systems at the station $x_\perp/\delta_0 = 650$. It can be noted that the maximum value of the x derivative decreases by two orders of magnitude, and moreover, the spatial distribution of the derivatives exhibits a distinctly different shape when represented in a coordinate system closely aligned with the crossflow vortex axis. The resulting domain, oriented to coincide with the direction $\theta_{\min}$ and used for the stability analysis, is displayed in Fig. 9 with a light green color. Also shown is a close-up view of the domain that displays the stationary crossflow vortices visualized by an isosurface of the λ_2 criterion [38]. The vortex turns out to be completely contained within the domain employed for the stability analysis, confirming that the crossflow vortex axis is closely aligned in the direction of the least gradient of the distorted base flow.

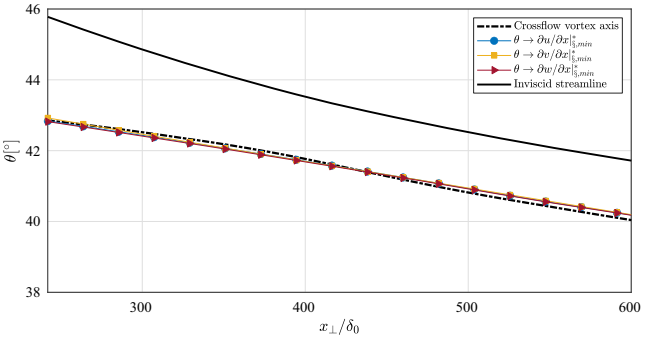

Fig. 6 Chordwise development of the angle of the inviscid streamline (solid black line), the angle of the crossflow vortex axis (dash-dotted black line), and the ones corresponding to the minimum out-of-plane rms derivative.

2. *LST-2D and PSE-3D Methodologies*

In this work, the incompressible LST-2D and PSE-3D methodologies formulated in a nonorthogonal coordinate system are employed to address the instability characteristics of flows that are inhomogeneous in at least two spatial directions. Both are linear theories that superpose an unsteady perturbation of small amplitude onto an undisturbed steady base flow. Accordingly, the flow quantities $\boldsymbol{q} = (u, v, w, p)^T$ are decomposed into a steady part $\bar{\boldsymbol{q}} = (\bar{u}, \bar{v}, \bar{w}, \bar{p})^T$, which is commonly known as the base flow, and into a fluctuating component with small-amplitude ε, denoted as $\tilde{\boldsymbol{q}} = (\tilde{u}, \tilde{v}, \tilde{w}, \tilde{p})^T$:

$$\boldsymbol{q}(x, y, z, t) = \bar{\boldsymbol{q}}(x, y, z) + \varepsilon\tilde{\boldsymbol{q}}(x, y, z, t), \quad \varepsilon \ll 1 \tag{2}$$

where (x, y, z) represent the nonorthogonal coordinate system introduced earlier. The LST-2D relies on the parallel flow assumption. Therefore, two spatially inhomogeneous directions have to be resolved

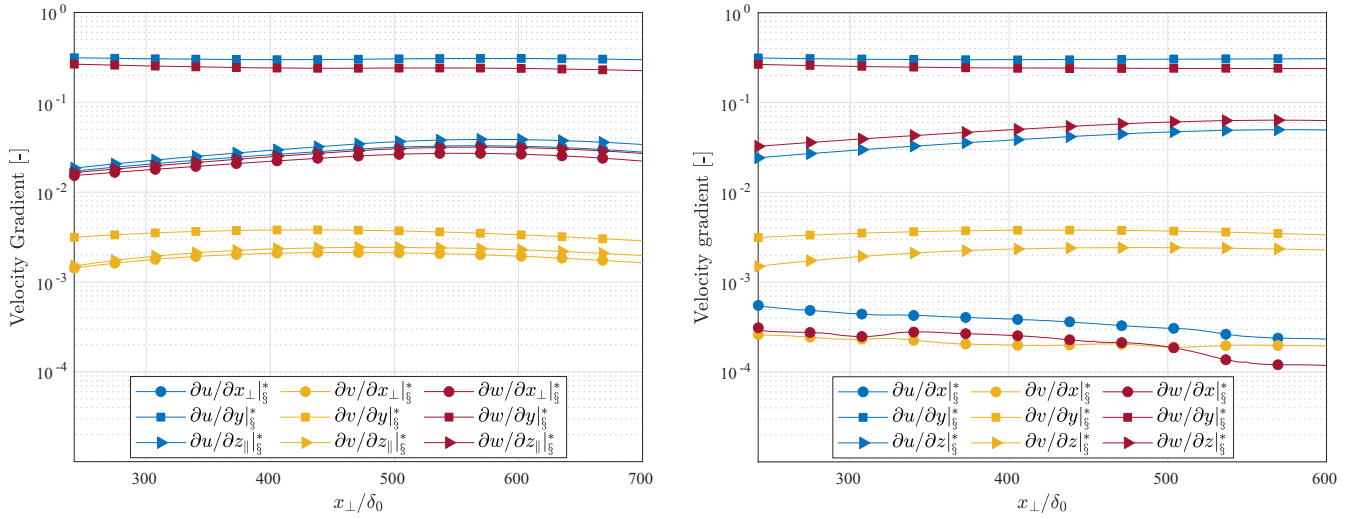

a) Orthogonal $(x_\perp, y, z_\parallel)$ coordinate system **b) Nonorthogonal (x, y, z) coordinate system**

Fig. 7 Rms of the velocity gradients in a) the chordwise direction, and in b) the direction of least variation for the out-of-plane derivative, i.e., $\theta_{\min}$ at the station $x_\perp/\delta_0 = 650$.

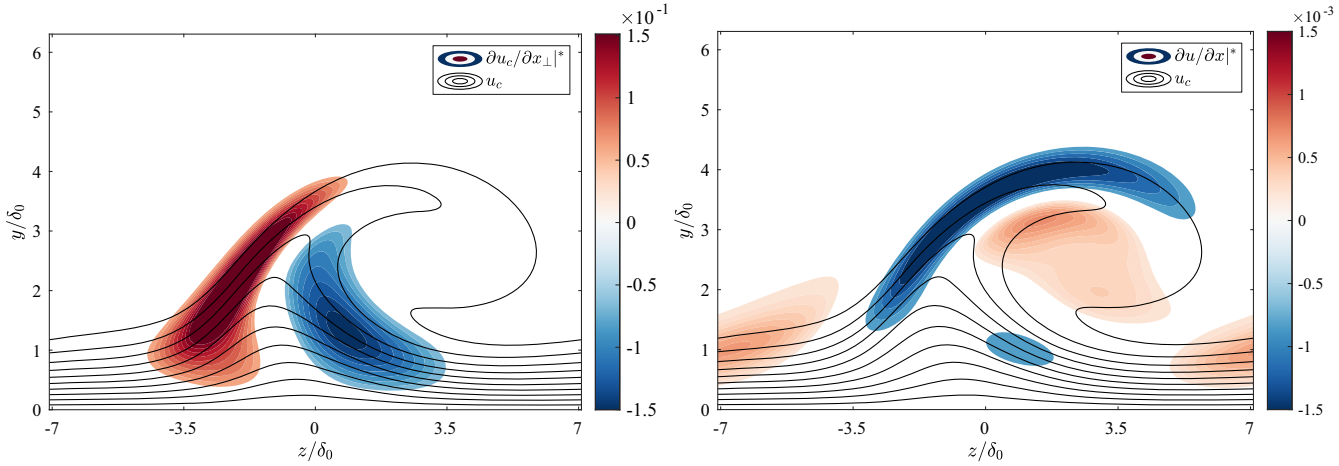

a) Orthogonal ($x_\perp, y, z_\parallel$) coordinate system

b) Nonorthogonal (x, y, z) coordinate system

Fig. 8 a) Out-of-plane derivative in the chordwise direction $x_\perp$, and b) x direction. Isolines of the $x_\perp$-velocity component of the distorted base flow are in solid black.

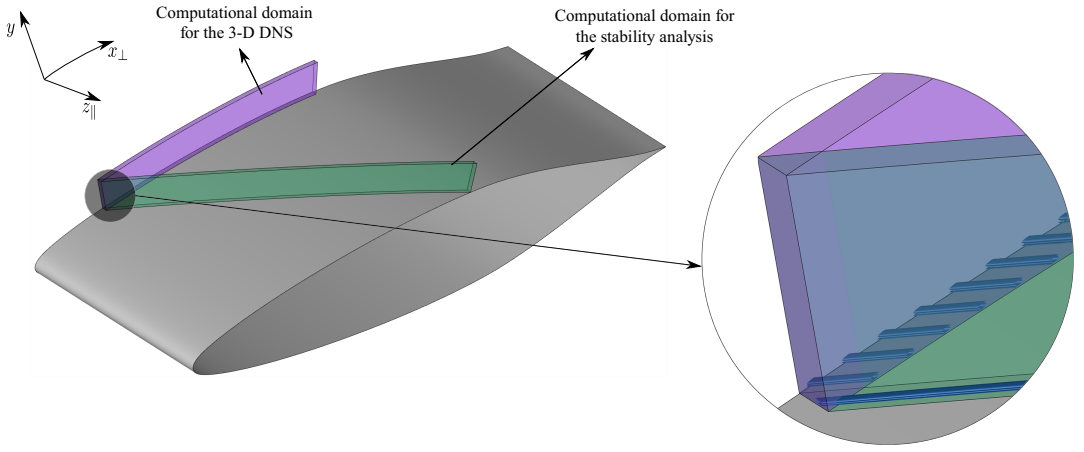

Fig. 9 Computational domain for the 3-D DNS in violet and the domain employed for the stability analysis in green with a close-up of the two domains in which the stationary crossflow vortex is visualized by an isosurface of the λ_2 criterion ($\lambda_2 = -2 \cdot 10^6$).

simultaneously in a plane, whereas spatial homogeneity in the streamwise direction is assumed, that is, $\bar{\boldsymbol{q}} = \bar{\boldsymbol{q}}(y, z)$ holds. The corresponding ansatz for the perturbation term is

$$\tilde{\boldsymbol{q}}(x, y, z, t) = \hat{\boldsymbol{q}}(y, z) \exp[i(\alpha x - \omega t)] + \text{c.c.} \tag{3}$$

where $\hat{\boldsymbol{q}} = [\hat{u}, \hat{v}, \hat{w}, \hat{p}]^T$ represents the complex-valued amplitude function in the plane yz, and c.c. denotes the complex conjugate. This work utilizes the spatial framework and therefore α is a complex number and represents the streamwise wavenumber in the nonorthogonal coordinate system, and ω is real and represents the circular frequency of the mode. The real part of α represents the wavenumber of $\tilde{q}$ along the streamwise direction x with wavelength $\lambda_x = 2\pi/\alpha_r$, whereas the imaginary part is related to the growth rate, that is, σ:

$$\sigma = -\alpha_i \tag{4}$$

where $\alpha_i < 0$ means that the perturbation grows exponentially in the streamwise direction. The LST-2D equations can be formulated as a two-dimensional generalized eigenvalue problem, which is solved with the iterative implicitly restarted Arnoldi algorithm. On the other hand, the PSE-3D relaxes the parallel flow assumption and allows for slow variation of the base flow, the amplitude function $\hat{\boldsymbol{q}}$, and the wavenumber α along the x direction. Hence, the following ansatz for the disturbance terms is considered:

$$\tilde{\boldsymbol{q}}(x, y, z, t) = \hat{\boldsymbol{q}}(x, y, z) \exp\left[i\left(\int_x \alpha(x)\,\mathrm{d}x - \omega t\right)\right] + \text{c.c.} \tag{5}$$

In this case, the spatial growth rate σ consists of two contributions. The first accounts for the exponential part of the perturbation ansatz, whereas the second takes into account the growth associated with the streamwise variation of the amplitude function:

$$\sigma = -\alpha_i + \frac{\partial}{\partial x} \ell_n\left(\sqrt{E}\right) \tag{6}$$

where E is the total kinetic energy:

$$E = \int_y \int_z (|\hat{u}|^2 + |\hat{v}|^2 + |\hat{w}|^2)\,\mathrm{d}y\,\mathrm{d}z \tag{7}$$

Substituting the PSE-3D ansatz into the linearized Navier–Stokes equation, introducing a scale separation between the weak variation in the streamwise direction and the strong variation in the wall-normal direction and neglecting terms of order ($\mathcal{O}(1/Re^2)$), leads to the nonlocal linear stability equations. Those are expressed in a compact form as

$$\boldsymbol{A}\hat{\boldsymbol{q}} + \boldsymbol{B}\frac{\partial \hat{\boldsymbol{q}}}{\partial y} + \boldsymbol{C}\frac{\partial^2 \hat{\boldsymbol{q}}}{\partial^2 y} + \boldsymbol{D}\frac{\partial \hat{\boldsymbol{q}}}{\partial z} + \boldsymbol{E}\frac{\partial^2 \hat{\boldsymbol{q}}}{\partial^2 z} + \boldsymbol{F}\frac{\partial^2 \hat{\boldsymbol{q}}}{\partial y \partial z} + \boldsymbol{G}\frac{\partial \hat{\boldsymbol{q}}}{\partial x} = 0 \tag{8}$$

where the matrices $\boldsymbol{A}$, $\boldsymbol{B}$, $\boldsymbol{C}$, $\boldsymbol{D}$, $\boldsymbol{E}$, $\boldsymbol{F}$, and $\boldsymbol{G}$ contain the coefficients of the PSE-3D system of equations. In the PSE ansatz, both the amplitude function and the wavenumber α depend on the x direction. Therefore, an additional equation is required to remove this ambiguity. The following equation, which enforces the requirement for the PSE approximation that the amplitudes change slowly in the streamwise direction, is employed here [39]:

$$\int_y \int_z \left(\hat{u}^\dagger \frac{\partial \hat{u}}{\partial x} + \hat{v}^\dagger \frac{\partial \hat{v}}{\partial x} + \hat{w}^\dagger \frac{\partial \hat{w}}{\partial x} + \hat{p}^\dagger \frac{\partial \hat{p}}{\partial x} \right) \mathrm{d}y \, \mathrm{d}z = 0 \tag{9}$$

where $(\cdot)^\dagger$ indicates the complex conjugate. Starting from Eq. (8), four different subsets of equations can be derived. Neglecting the streamwise derivatives of the amplitude function, that is, $\partial \hat{\boldsymbol{q}}/\partial x = 0$ in Eq. (8), and those of the base flow, leads to the *local* parallel LST-2D. In this work, the parallel LST-2D also includes the base flow wall-normal velocity component. In literature, there is no consensus on whether it should be included in the equations and it appears to be dependent on the problem under investigation. For instance, Di Giovanni and Stemmer [40] analyzed the instabilities developing in the wake of spanwise periodic roughness elements, employing an LST-2D approach in which the wall-normal velocity component is neglected, and they found that this methodology provides a good enough agreement between the instability computations and DNS. On the other hand, we found that neglecting the base flow wall-normal velocity component for analyzing the development of secondary instabilities of stationary crossflow vortices did not result in a satisfactory agreement with DNS, which is why it is taken into account in the parallel LST-2D computations shown here. These findings are consistent with the results of Malik and Chang [41], who found that dropping the wall-normal velocity of the base flow significantly increased secondary amplification rates. The parallel flow assumption also implies that the base flow is periodic in the direction orthogonal to the crossflow vortex axis (not only in the direction parallel to the leading edge) and therefore this approach can be formulated in an orthogonal vortex-aligned coordinate system with the x direction along the vortex axis and the z direction perpendicular to the latter. This kind of coordinate system has been widely employed in the past to study the evolution of secondary perturbations of crossflow vortices [15,16,19,23]. The inclusion of streamwise base flow gradients, instead, yields the *local* nonparallel LST-2D set of equations. On the other hand, the *nonlocal* parallel PSE-3D neglects only the terms related to the streamwise variation of the base flow, retaining the upstream history of the amplitude functions through their streamwise gradient. Finally, when the complete set of equations is considered, the *nonlocal* nonparallel PSE-3D problem is solved. The *local* parallel LST-2D and the *nonlocal* nonparallel PSE-3D are the methodologies that are employed the most in literature. When parallel/nonparallel is not explicitly specified in the text, these approaches are used here for the instability computations. The two intermediate steps are introduced to separate the *local/nonlocal* and parallel/nonparallel effects and investigate their contribution separately on the instability computations when different out-of-plane directions are considered (see Sec. IV.D). The PSE-3D set of equations constitutes an initial boundary-value problem that can be solved by a streamwise marching procedure, which requires the information of the upstream disturbance flow in order to advance downstream. The *nonlocal* PSE-3D computation typically is started with a solution from an LST-2D eigenvalue computation (see [39,42] for more details on the LST-2D and PSE-3D for curvilinear orthogonal coordinate systems). In Sec. IV, the instability results are presented in terms of the integrated growth rate (n-factor), which is defined as follows:

$$n = \int_{x_0}^{x} \sigma \, \mathrm{d}x' \tag{10}$$

where σ represents the growth rate in the nonorthogonal coordinate system and x' represents a dummy integration variable for the out-of-plane x direction. To solve the LST-2D and PSE-3D equations, it is necessary to define appropriate boundary conditions for the disturbance variables. The no-slip condition is imposed at the wall ($y = 0$) by setting the velocity perturbations to zero. In the wall-normal direction, the perturbations are ensured to decay by imposing a homogeneous Dirichlet condition at the upper boundary. This boundary is placed far away from the wall to avoid any influence on the instability characteristics. Finally, the periodicity is exploited at the lateral boundaries by applying the periodic boundary condition to all involved variables. The wall-normal and spanwise directions are discretized using a stable finite-differences scheme of high order (FD-q), developed in [43]. The method is based on piecewise polynomial interpolation of degree $q \leq J$ on a nonuniform grid point distribution, where $J + 1$ is the total number of grid points in the corresponding spatial direction. The nonuniform grid point distribution, which lies in the interval $[-1\ 1]$, usually does not coincide with the physical domain, so a proper mapping must be applied. In the spanwise direction, a biquadratic mapping [23] has been employed, which is a generalization of the mapping used by Malik [44]. The grid points are equally distributed in three intervals $[0, z_{i1}]$, $[z_{i1}, z_{i2}]$, and $[z_{i2}, z_{\max}]$. This type of distribution allows the clustering of more points in the middle of the domain, where the amplitude function is expected to have the largest gradients while keeping a cosine distribution toward the lateral boundaries to avoid oscillations. In the wall-normal direction, a similar approach has been used that allows a flexible distribution of points in order to cluster them at different wall-normal heights. In the PSE-3D computations, the streamwise derivative is discretized via an implicit first-order backward Euler scheme. Grid convergence was obtained with a grid of 101×121 points in the spanwise and wall-normal directions, respectively, and applying a value of 8 for q.

IV. Secondary Instabilities

This section presents a comparative analysis of DNS and LST-2D/PSE-3D results for the unsteady perturbations evolution. Additionally, the effect of selecting different out-of-plane directions for the instability computations is investigated.

The nondimensional power spectral density P^* of the chordwise velocity fluctuations for two selected probe positions from the DNS (displayed by the green circle and blue triangle in the inset of Fig. 10) at the chordwise station $x_\perp/\delta_0 = 584$ are plotted in Fig. 10. The velocity signals obtained from the DNS, comprising 3400 samples at a sampling rate of 25,000 Hz, were analyzed using Welch's method [45]. This involved dividing the data into segments, with each segment windowed by a Hann function. A total of 10 periodograms were computed and averaged to estimate the power spectral density, with a 50% overlap between consecutive segments. The power spectral density lines in the figure are color-coded to match the color of the markers in the contour inset, which depicts the rms distribution of the chordwise velocity component of the fluctuations from the DNS. Figure 10 reveals that the fluctuations occur in regions associated with Type I and Type III secondary instability, as discussed in Sec. I. The chordwise station at $x_\perp/\delta_0 = 584$ is chosen as an illustrative example because it is located slightly upstream of the transition location in the DNS, thereby providing an indication of the mechanisms playing a relevant role in the transition process. The spectral analysis of the two probes within the different fluctuation regions reveals a marked dominance of distinct spectral content: the inner upwelling region (marked by the blue color) is characterized by pronounced spectral energy around $f = 900$ Hz, whereas the fluctuations in the outer region of the upwelling flow (indicated with the green color) predominantly feature higher frequencies. Consequently, the frequencies of $f = 900$ Hz and $f = 2200$ Hz, representative of Type III and Type I secondary instability modes, respectively, are selected for the subsequent instability analysis and comparison with DNS. In particular, Sec. IV.A portrays the impact of surface curvature on a Type III secondary instability, and then a comparison with DNS data is displayed in Secs. IV.B and IV.C. In view of the discussion presented in Sec. III.B.1,

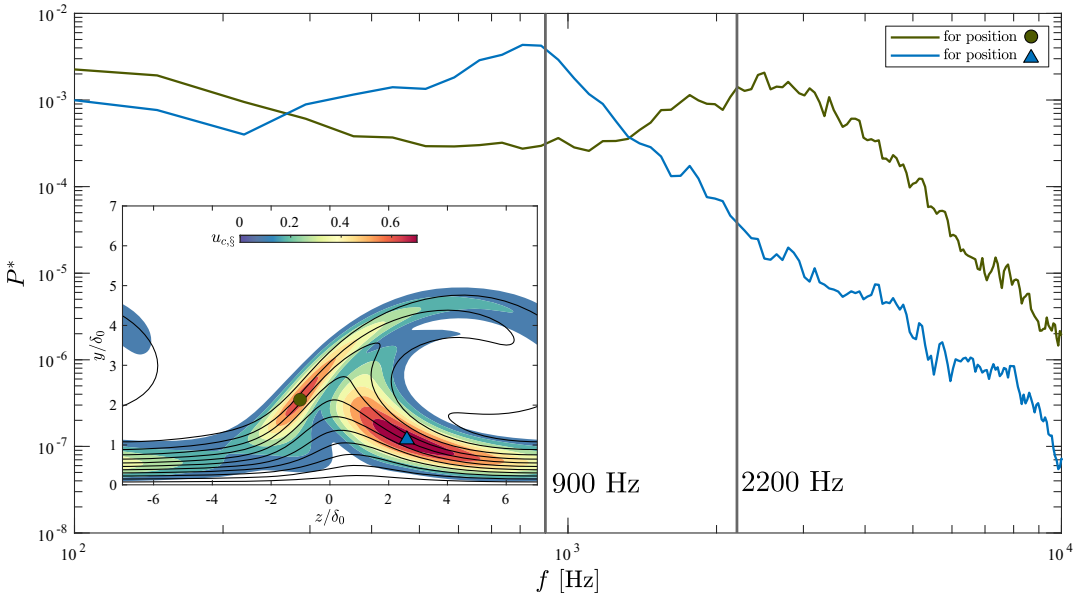

Fig. 10 Nondimensional power spectral density of the chordwise velocity fluctuations for two selected probe positions marked by the green circle and blue triangle in the inset.

on how the choice of the x direction influences the rms of the base flow derivatives, the instability computations shown in Sec. IV.A, IV.B, and IV.C are carried out employing $\theta_{\min}$ as x direction. On the other hand, the effect of different x-direction choices on the instability computations is investigated in Sec. IV.D.

Note that, because the secondary instabilities of stationary crossflow vortices are of convective nature, as demonstrated by Wasserman and Kloker employing DNS [14] and theoretically by Koch [46], a spatial approach (see Sec. III.B.2) is more appropriate and is employed here for the instability computations. However, solving the spatial eigenvalue problem is computationally more expansive than solving the eigenvalue system in the temporal framework. Therefore, previous authors have employed the well-known Gaster transformation [47] to relate the temporal and spatial growth rates:

$$-\alpha_i = \omega_i / c_{g,r} \tag{11}$$

where $c_{g,r} = \partial\omega_r/\partial\alpha_r$ denotes the real part of the group velocity. The relation was derived assuming a small temporal growth rate but it has been successfully applied by previous authors to study the roughness-induced instabilities in high-speed boundary layers [22,48] or to analyze the development of the secondary instabilities of Görtler vortices [49]. Furthermore, Malik et al. [16] and Koch et al. [15] extended the Gaster's transformation to convert temporal growth rate data to spatial growth rates for secondary instabilities of crossflow vortices. In particular, Koch et al. [15] demonstrated its accuracy for such cases. Recently, Gaster's transformation was revisited by Xu et al. [50], who proposed first- and second-order transformations, which are less restrictive than the former one. In the present work, both the Gaster's transformation and the newly developed spatiotemporal relationships were employed (not shown) to check their validity for the development of secondary instabilities of stationary crossflow vortices computed in a nonorthogonal coordinate system. The comparison between spatial growth rates obtained by means of the transformations of Gaster and Xu et al. and the ones computed by solving the spatial eigenvalue problem revealed an overall good agreement. Note that the real part of the group velocity ($c_{g,r}$) in the nonorthogonal x direction is employed for the transformation.

A. Impact of Surface Curvature

This section analyzes the effect of surface curvature on the secondary instabilities. Figure 11a portrays the impact of chordwise convex surface curvature on the spatial growth rate of an LST-2D computation, for a Type III secondary instability at two different positions computed with rectilinear (surface curvature neglected) and curvilinear (surface curvature included) metric. Figure 11b depicts the impact of convex surface curvature on the spatial growth rate of a PSE-3D computation for a frequency $f = 900$ Hz as function of the chordwise direction. As evident from the figure, the convex airfoil curvature has a nonnegligible stabilizing impact

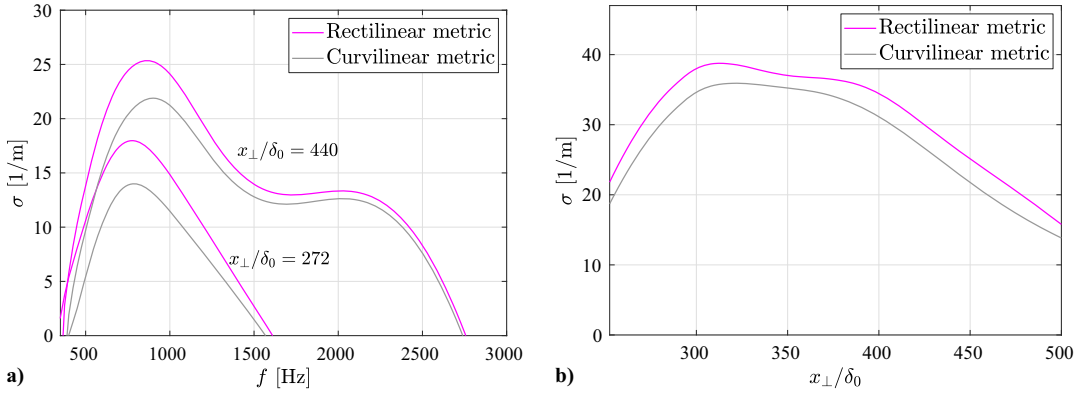

Fig. 11 Impact of convex surface curvature on the spatial growth rate of a Type III secondary instability. a) σ as a function of frequency for an LST-2D computation, and b) σ as a function of $x_\perp/\delta_0$ at a frequency $f = 900$ Hz for a PSE-3D solution.

on the growth rate of the secondary instability, displaying a similar trend as for the primary crossflow instability [51]. The impact of convex surface curvature on Type I secondary instabilities follows a pattern similar to that observed for the Type III instabilities. Due to its stabilizing impact, surface curvature will be considered for all the following computations.

B. Perturbation Evolution at $f = 900$ Hz

In this section, the focus is on the development of the unsteady perturbation at a frequency of $f = 900$ Hz for which a Type III secondary instability mechanism prevails. Figure 12 presents a comparison between the DNS results, depicted by filled isocontours, and those obtained from LST-2D (Fig. 12a) and PSE-3D (Fig. 12b), illustrated with purple isolines, for the normalized magnitude of the chordwise velocity component of the amplitude function, that is, $|\hat{u}_c/\hat{u}_{c,\max}|$. The results from the instability computations are transformed back to the orthogonal curvilinear $(x_\perp, y, z_\parallel)$ coordinate system for a direct comparison with the DNS results. The amplitude function closely resembles previous results from theoretical, numerical, and experimental works [15,19,23,52], where unsteady perturbations of this particular shape, located close to the wall, are classified as Type III secondary instabilities. As noted earlier, this instability is related to low-frequency traveling crossflow instabilities modulated by the presence of the stationary crossflow vortex.

Both the LST-2D and PSE-3D computations are able to recover the main features of the unsteady perturbation, accurately reflecting the mode shape and location, with a strong overall agreement with the DNS results at station $x_\perp/\delta_0 = 430$, as shown in Fig. 12. Although there is a notable agreement, the LST-2D results appear to deviate slightly. It should be noted that the LST-2D solution is obtained by solving a generalized eigenvalue problem at the specific $x_\perp$ station, whereas the PSE-3D solution is obtained by a marching procedure, which accounts for the nonparallel effects on the amplification of the secondary instability modes. The PSE-3D starts at station $x_\perp/\delta_0 \approx 300$, which is far enough upstream to ensure that the PSE-3D results at the station $x_\perp/\delta_0 = 430$ are unaffected by the initial transient. The comparison is further carried out by comparing the DNS results with the PSE-3D instability results across different stations, as shown in Fig. 13. It is observed that the secondary perturbation, initially situated in the inner upwelling region of the stationary crossflow vortex, shifts away from the wall toward the upwash side of the stationary crossflow vortex as it progresses downstream along the streamwise direction. The PSE-3D results show an overall good agreement with the DNS data for all downstream stations. Casacuberta et al. [28], in their two-dimensional eigenvalue computations for the development of secondary instabilities in a swept-wing-type boundary layer over a flat plate, reported that the Type III mode from the instability computation tends to extend more toward the shoulder of the stationary crossflow vortex with respect to the results observed from the DNS. Moreover, their computations employing a *local* approach not only display a major disagreement on the upper side of the eigenfunction, but an increasing disagreement also in the near-wall region, as the perturbation evolves downstream. The results in Fig. 13 exhibit only

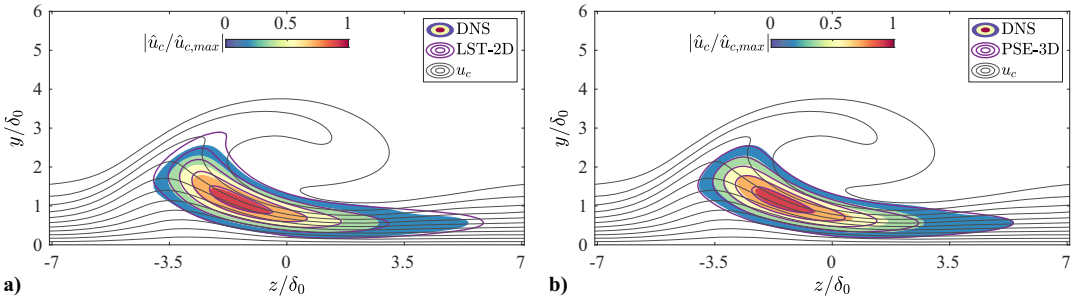

Fig. 12 Normalized magnitude of the chordwise velocity amplitude function ($|\hat{u}_c/\hat{u}_{c,\max}|$) for a Type III secondary instability at a frequency of 900 Hz, shown at the station $x_\perp/\delta_0 = 430$.

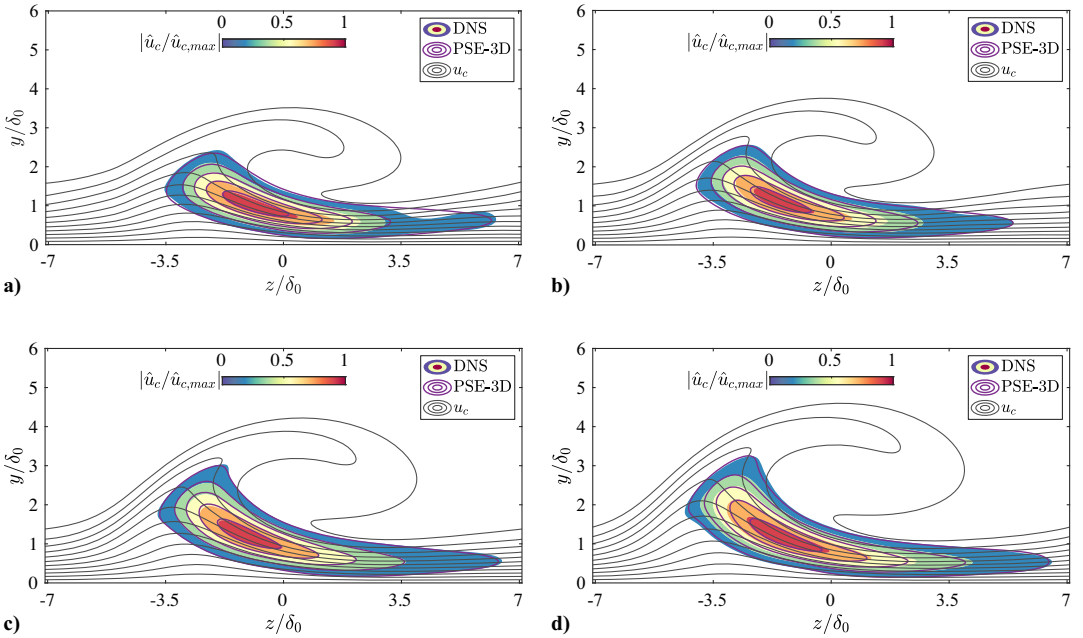

Fig. 13 Normalized magnitude of the chordwise velocity amplitude function ($|\hat{u}_c/\hat{u}_{c,\max}|$) for a Type III secondary instability at a frequency of 900 Hz, shown at the stations a) $x_\perp/\delta_0 = 390$, b) $x_\perp/\delta_0 = 439$, c) $x_\perp/\delta_0 = 458$, and d) $x_\perp/\delta_0 = 490$.

minor deviations with respect to the DNS results, and the lower discrepancy on the shape of the amplitude function might be attributed to the use of a PSE-3D methodology in the current analysis that incorporates the streamwise derivative of the base flow and of the amplitude functions, resulting in enhanced accuracy. Furthermore, it is emphasized that the perturbations extracted from the DNS do not necessarily consist of a pure secondary instability mode, but may include contributions from other perturbations at the same frequency because in the DNS they originate from a random forcing. This may contribute to the small differences noted between PSE-3D and DNS results and it holds also for the comparisons shown in Sec. IV.C.

The integrated growth rate, that is, the n-factor, is shown in Fig. 14. Note that the n-factor computations in DNS and the instability analyses are based on the integral of the disturbance kinetic energy across the plane yz. In the DNS, a disturbance strip at the wall near the inflow introduces a wide spectrum of frequencies, necessitating a transient phase before the emergence of a distinct Type III secondary instability, which is observed starting from $x_\perp/\delta_0 \approx 390$. From this station on, a clear Type III secondary instability can be recognized in the DNS, which facilitates a quantitative comparison with the results from the instability computations. The n-factor curves from the instability computations have been normalized at this position for comparison with the DNS data. It can be seen that the parallel LST-2D computation strongly underestimates the n-factor curve of the DNS over the entire domain. The same holds for the nonparallel LST-2D that additionally takes into account the streamwise gradients of the base flow quantities. On the other side, the parallel PSE-3D and the PSE-3D results align closely with the exponential growth of the secondary instability. The PSE-3D computation is the only one displaying an excellent agreement, at least up to station $x_\perp/\delta_0 \approx 520$. Choudhari et al. [27] also observed in their stability computations a strong underprediction of the n-factors when solving the two-dimensional eigenvalue problem compared to the plane-marching PSE-3D approach. It can be noted that the inclusion of the streamwise gradient of the base flow quantities does not seem to play a significant role because the parallel and nonparallel LST-2D computations are close to each other, and the same holds for the PSE-3D.

Beyond $x_\perp \approx 520$, the two curves start to deviate, probably due to nonlinear interactions of secondary instabilities in the DNS computation, precluding further comparison with linear instability results. Figure 15 visualizes the instability, based on PSE-3D data, through two isosurfaces of the normalized real part of the streamwise velocity component of the amplitude function. Furthermore, the insets display a zoom at three different stations $x_\perp/\delta_0 = 260$, $x_\perp/\delta_0 = 420$, and $x_\perp/\delta_0 = 560$. As already seen in Fig. 13, the amplitude function shifts toward the upwash side of the crossflow vortex as it progresses in the streamwise direction. As can be seen in Fig. 15, the isosurfaces, initially in the near-wall shear layer, twist and follow the direction of rotation (clockwise) of the crossflow vortex as they move downstream.

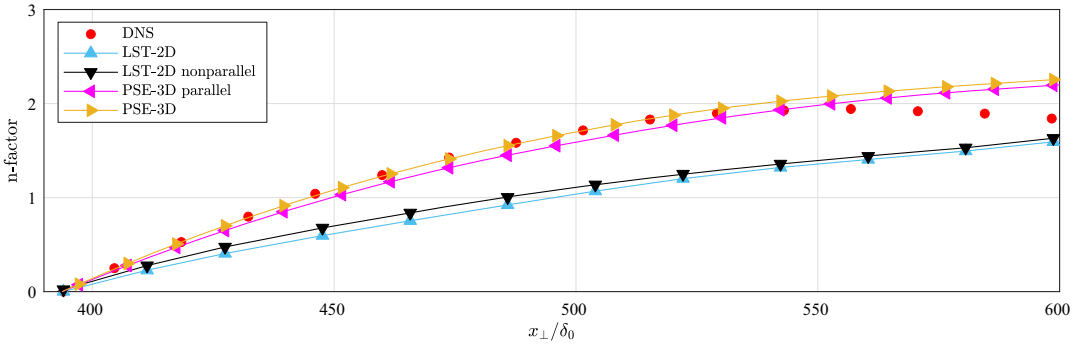

Fig. 14 N-factor curves vs $x_\perp/\delta_0$ for a Type III secondary instability of f = 900 Hz.

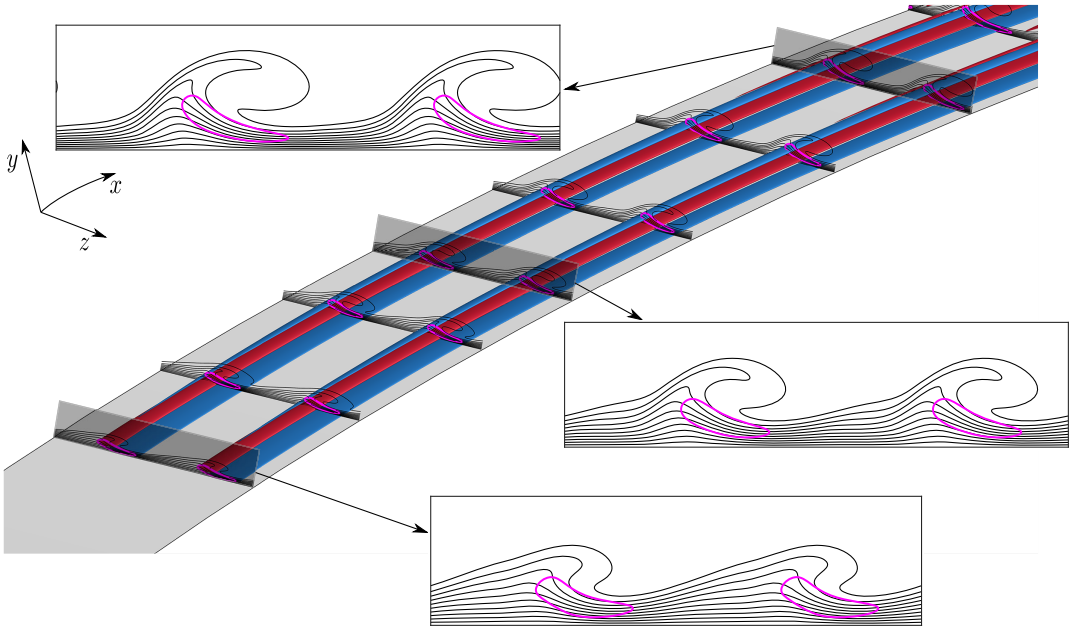

Fig. 15 Type III secondary instability at f = 900 Hz represented by red (positive) and blue (negative) isosurfaces of the normalized real part of the streamwise velocity component amplitude function ($\hat{u}_r/\hat{u}_{r,\max} = \pm 0.2$). Isolines of the streamwise velocity component of the distorted base flow in solid black and normalized magnitude of the streamwise velocity amplitude function represented by a purple isoline ($|\hat{u}/\hat{u}_{\max}| = 0.5$).

C. Perturbation Evolution at $f = 2200$ Hz

In the following section, the evolution of the unsteady perturbation at a frequency of 2200 Hz is analyzed. This frequency is dominated by a perturbation localized on the shoulder of the stationary crossflow vortex. Such perturbations are associated with a Type I secondary instability in the literature [9,15,16,19,23,52]. Figure 16 shows a comparison between the DNS results and those obtained from a) LST-2D and b) PSE-3D for the normalized magnitude of the chordwise velocity component of the amplitude function. The secondary instability is located on the upwash side of the stationary crossflow vortex and the location of the maximum perturbation coincides with the minimum (negative maximum) of the spanwise shear, that is, $\partial u/\partial z$. Similar to the Type III instability, both LST-2D and PSE-3D results show an overall good agreement in terms of amplitude function, even though the PSE-3D computation aligns more closely with the DNS results. The agreement of the PSE-3D results with the DNS is further confirmed at several stations downstream, as plotted in Fig. 17. Figure 18 shows the evolution of the n-factor curve along $x_\perp$. As for the instability results for $f = 900$ Hz, in the DNS there is a transient phase before the emergence of a distinct Type I secondary instability, which is observed starting from $x_\perp/\delta_0 \approx 370$. The n-factor curves from the instability computations have been normalized at this position for comparison with the DNS data. As the Type III secondary instability, it is noteworthy that both the parallel and nonparallel LST-2D results significantly underpredict the integrated growth rate,

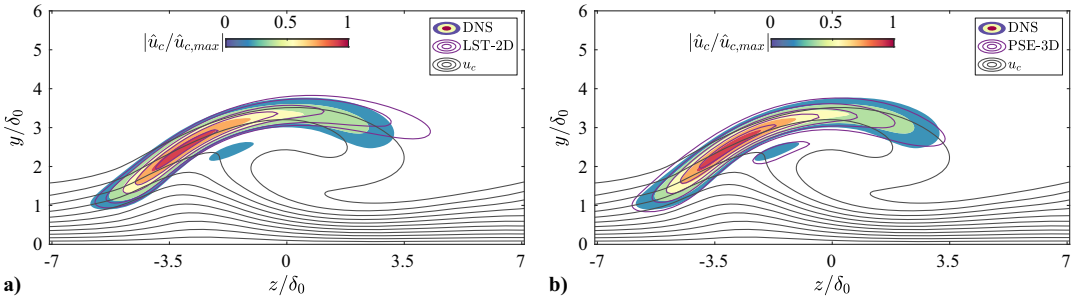

Fig. 16 Normalized magnitude of the chordwise velocity amplitude function ($|\hat{u}_c/\hat{u}_{c,\max}|$) for a Type I secondary instability at a frequency of 2200 Hz, shown at the station $x_\perp/\delta_0 = 390$.

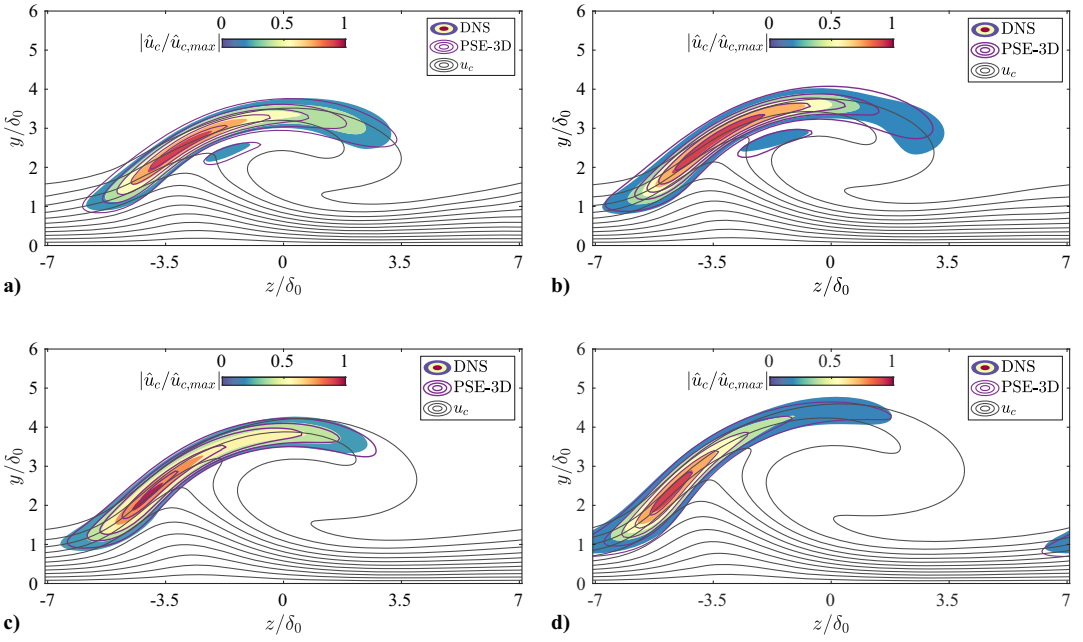

Fig. 17 Normalized magnitude of the chordwise velocity amplitude function ($|\hat{u}_c/\hat{u}_{c,\max}|$) for a Type I secondary instability at a frequency of 2200 Hz, shown at the stations a) $x_\perp/\delta_0 = 390$, b) $x_\perp/\delta_0 = 439$, c) $x_\perp/\delta_0 = 458$, and d) $x_\perp/\delta_0 = 490$.

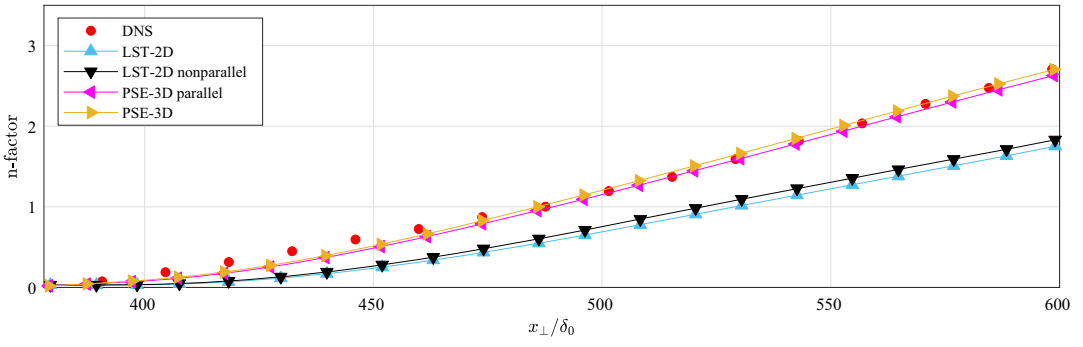

Fig. 18 N-factor curves vs $x_\perp/\delta_0$ for a Type I secondary instability for a frequency of 2200 Hz.

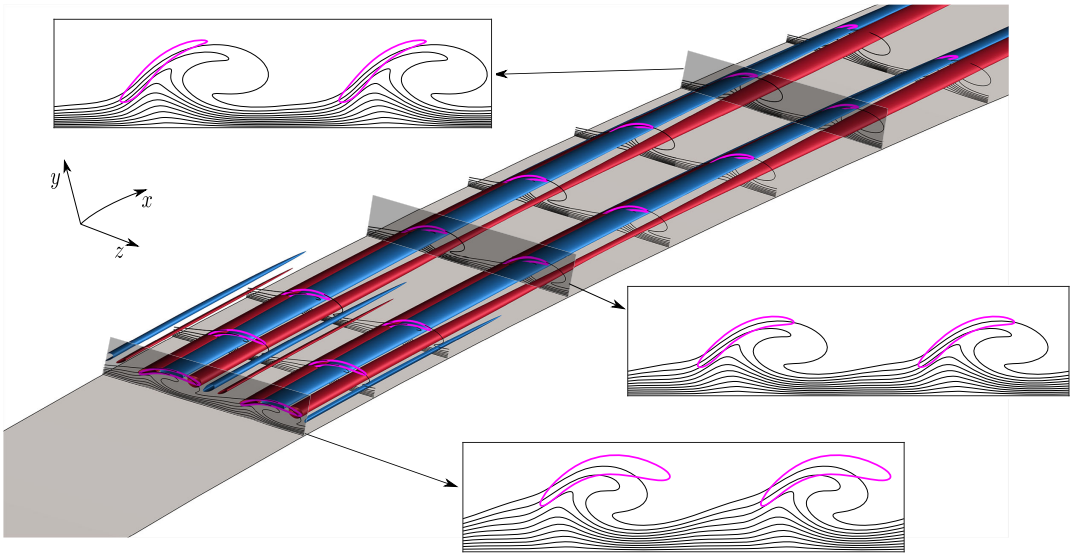

Fig. 19 Type I secondary instability at 2200 Hz represented by red (positive) and blue (negative) isosurfaces of the normalized real part of the streamwise velocity amplitude function ($\hat{u}_r/\hat{u}_{r,\max} = \pm 0.2$). Isolines of the streamwise velocity component of the distorted base flow in solid black and normalized magnitude of the streamwise velocity amplitude function represented by a purple isoline ($|\hat{u}/\hat{u}_{\max}| = 0.5$).

whereas the parallel PSE-3D and the PSE-3D results are much closer to those from the DNS, with the PSE-3D computation showing the overall best agreement. Again, Fig. 19 depicts two isosurfaces of the real part of the normalized streamwise velocity component of the amplitude function, providing a visual representation of the perturbation structures at the specified frequency. Additionally, the insets provide a zoom at three different stations $x_\perp/\delta_0 = 330$, $x_\perp/\delta_0 = 410$, and $x_\perp/\delta_0 = 540$.

D. Effect of Different Out-of-Plane Directions

In this section, we examine the effect of different out-of-plane directions when using the four different sets of equations introduced in Sec. III.B.2. The results presented in the two preceding sections were obtained using a coordinate system such that the x direction deviates from the chordwise direction by the angle $\theta_{\min}$. We investigate the unsteady perturbation evolution at a frequency of 900 Hz while considering variations in the out-of-plane direction, which translates into different integration paths for the n-factor evaluation. These paths are visualized as colored solid lines in Fig. 20, together with a schematic representation of the wing. The path considered for the n-factor computation in Figs. 14 and 18 is indicated by a light-blue solid line. Here, we explore slight deviations from this out-of-plane direction, specifically deviations of ± 0.5 deg, as well as the direction of the external inviscid streamline. The results for the selected integration paths are depicted in Fig. 21, which presents the n-factor curves for the a) LST-2D, b) the *local* nonparallel LST-2D, c) the *nonlocal* parallel PSE-3D, and d) PSE-3D. The four different sets of equations were considered to gain a better insight into the terms that significantly affect the results and to understand the sensitivity to the out-of-plane direction employed in computing the integrated growth rate. The parallel LST-2D results exhibit a

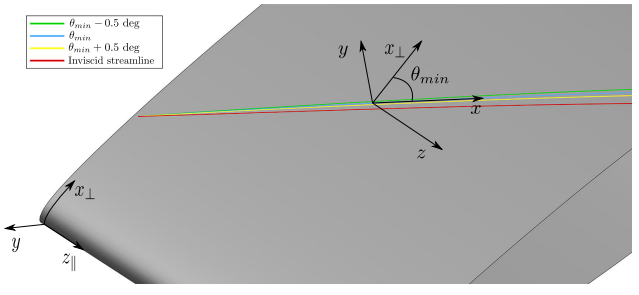

Fig. 20 Sketch of the wing and the different integration paths considered.

pronounced sensitivity to changes in the integration path; even slight deviations in the θ angle significantly influence the predicted n-factor. A variation of ± 0.5 around the angle θ, for which the rms $\partial u/\partial x|_{\S}$ is minimal, leads to a notable difference in the n-factor value, with a $|\Delta n|$ of approximately 0.5 at the end of the integration domain. Furthermore, the effect becomes even more pronounced when the inviscid external streamline direction is used as the integration path. The relationship between the angle of the inviscid streamline at the boundary-layer edge and the angle $\theta_{\min}$ is depicted in Fig. 6. It can be noted that they differ from each other by approximately 2-deg in the domain of interest. Choosing the streamline direction as x direction of the nonorthogonal coordinate system leads to an n-factor value that is approximately twice the value obtained from the direction $\theta_{\min}$ at the end of the computational domain.

The significant effect of the x direction on the n-factor results is partially explained by its influence on the spanwise and streamwise gradients of the base flow, which, in turn, drastically affects the growth rate. In Fig. 22, the rms of the streamwise, $\partial u/\partial x|^*_{\S}$, and spanwise, $\partial u/\partial z|^*_{\S}$, velocity gradients are shown for the four different out-of-plane marching directions as a function of $x_\perp/\delta_0$. A significant influence of the x direction on the rms of the spanwise shear can be noted. The spanwise gradients change with θ due to the interdependence between the x- and z direction in the nonorthogonal coordinate system (see Appendix). It can be noted that as the deviation from the direction $\theta_{\min}$ increases, the rms of the streamwise gradient becomes larger. In fact, it can be seen that the streamwise gradient, in the case where the out-of-plane direction is aligned with the inviscid streamline, is about four times larger than the same derivative computed along the direction of least variation over the full range of $x_\perp$. This discrepancy causes the modeling error in the LST-2D to become more pronounced, as this methodology assumes a negligible streamwise gradient. On the other hand, when we consider the *local* nonparallel LST-2D results, it can be seen that the inclusion of the base flow streamwise derivative has beneficial effects on the sensitivity of the n-factor results across the four different integration paths, leading to smaller differences at the end of the integrated curves. Additionally, when we consider the *nonlocal* parallel PSE-3D, including the upstream history of the amplitude function, it has a beneficial effect over the parallel LST-2D, displaying a sensitivity to the x direction slightly worse than the nonparallel LST-2D. As one can see, the slopes of the n-factor curves up to $x_\perp = 350$ in Fig. 21b are very similar, whereas the slopes up to the same location in Fig. 21a display a larger deviation, indicating that the sensitivity to the out-of-plane direction is mainly affected by the streamwise base flow gradients at the beginning of the integration path. On the other hand,

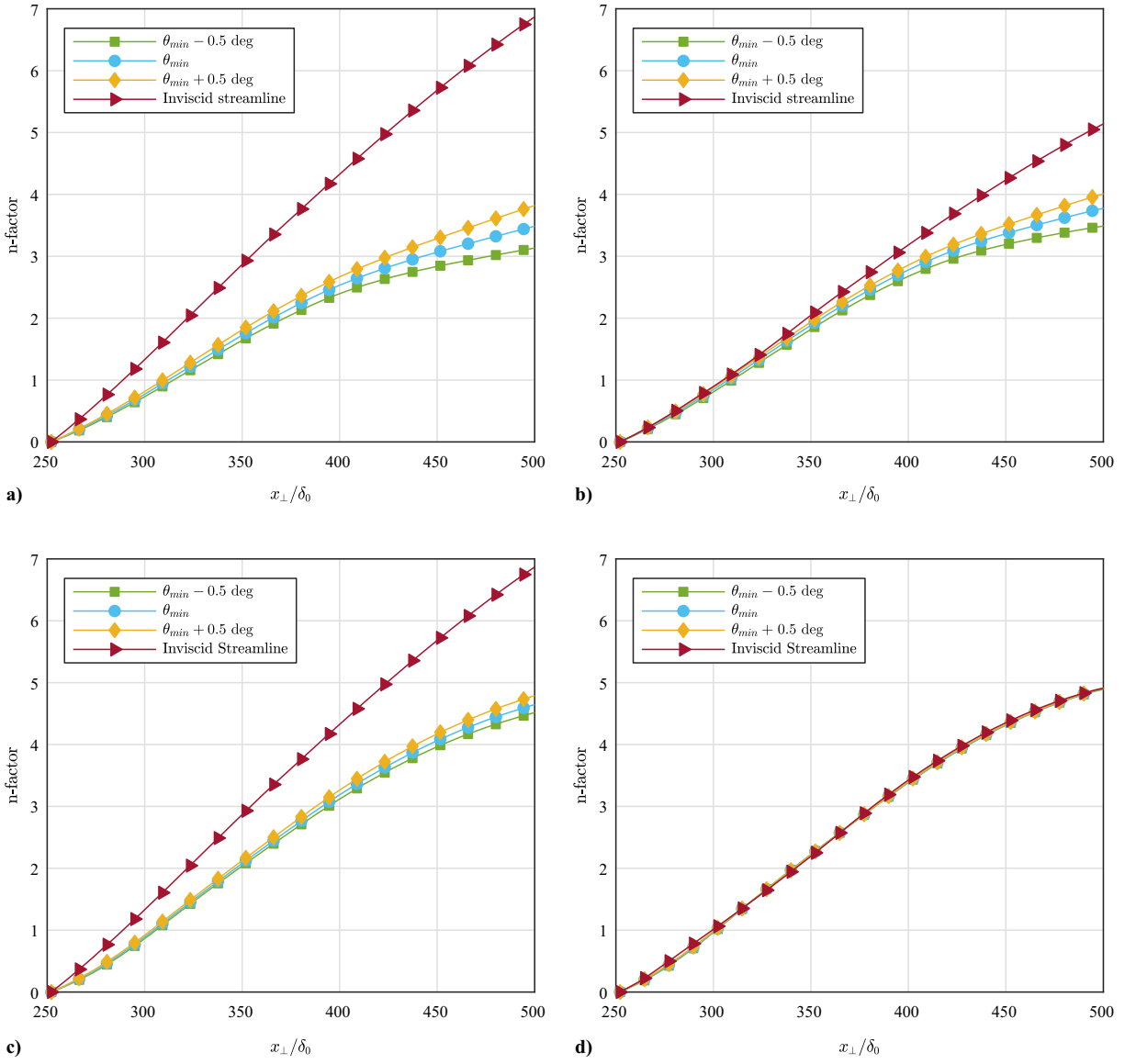

Fig. 21 N-factor curves vs $x_\perp/\delta_0$ of a Type III secondary instability for a frequency of 900 Hz. a) LST-2D, b) LST-2D nonparallel, c) PSE-3D parallel, and d) PSE-3D for different out-of-plane marching directions.

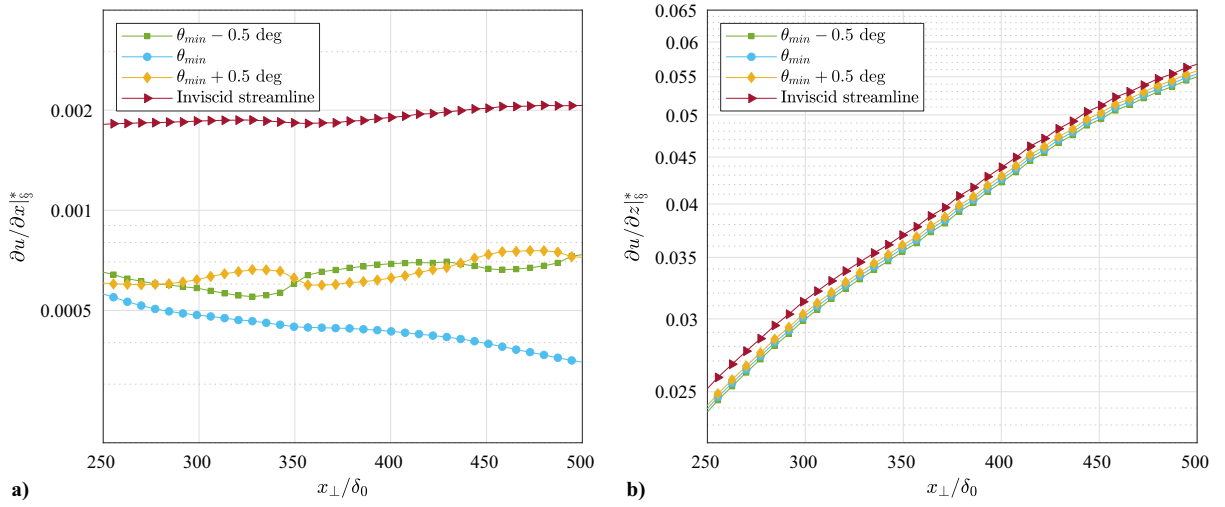

Fig. 22 a) Streamwise $\partial u/\partial x|^*_{\S}$, and b) spanwise $\partial u/\partial z|^*_{\S}$ velocity gradient for different out-of-plane directions.

Table 1 Sensitivity to the integration path: $|\Delta n|$ relative to the path θ_{min}

Path	LST-2D	LST-2D nonparallel	PSE-3D parallel	PSE-3D
$\theta_{min} - 0.5$ deg	0.33	0.23	0.14	0.001
$\theta_{min} + 0.5$ deg	0.35	0.27	0.13	0.002
Inviscid streamline	3.4	1.37	2.2	0.002

the inclusion of the streamwise gradients of the amplitude function plays an important role more downstream.

Finally, in contrast with the preceding numerical methodologies, the nonparallel PSE-3D results for the four distinct paths yield the same n-factor, despite the substantial variation in spanwise shear due to a change in the angle θ. This is attributed to both the inclusion of the streamwise gradient in the PSE-3D approach and of the upstream history of the perturbation, whereas those are neglected in the LST-2D methodology. Therefore, the use of a *nonlocal* nonparallel PSE-3D approach permits the selection of various marching directions without affecting the instability results. This is valid as long as the deviation from the direction θ_{min} is small because larger deviations result in larger gradients in the x direction, rendering the PSE-3D assumptions questionable. Finally, Table 1 provides a summary of the results in terms of $|\Delta n|$ among the three additional paths considered in this section and the one featuring θ_{min} at the station $x_\perp/\delta_0 = 500$.

V. Conclusions

In this work, a detailed quantitative comparative analysis between direct numerical simulation (DNS) and linear stability theory was conducted, examining the evolution of secondary unsteady disturbances in a crossflow-dominated incompressible boundary layer over an infinite swept wing. Specifically, the linear stability theory (LST-2D) and plane-marching linear parabolized stability equations (PSE-3D) methodologies formulated in a nonorthogonal coordinate system were employed to investigate the base flow, which is distorted by the action of finite-amplitude stationary crossflow vortices and exhibits strong inhomogeneity in the spanwise, wall-normal, and chordwise directions. The LST-2D and PSE-3D equations can handle the strong gradients in the wall-normal and spanwise directions. However, the strong gradient in the chordwise direction neither complies with the assumption of zero streamwise gradients of the LST-2D nor the slow variation in the marching direction of the PSE-3D when formulated in an orthogonal coordinate system. One initial challenge is to find the most suitable way to represent the base flow in the stability problem. In previous studies, discrepancies between DNS and various stability tools were attributed to simplifying assumptions required for the base flow used as input for stability analysis [19]. By adopting a nonorthogonal coordinate system, the periodicity of the base flow in a direction parallel to the leading edge is respected. Moreover, it allows for the selection of an out-of-plane direction, along which the base flow evolves slowly. This direction was found by minimizing the root mean square (rms) of $\partial u/\partial x$, and it has been referred to as θ_{min}.

The main focus of this study was to examine the evolution of unsteady secondary disturbances at frequencies of $f = 900$ Hz and $f = 2200$ Hz. The former frequency exhibits a dominant Type III mode located in the region close to the wall, at the location where the spanwise shear attains its maximum. On the other hand, the higher frequency corresponds to a Type I instability, which lies on the upwash side of the stationary crossflow vortex. The main results may be summarized as follows:

1) The excellent quantitative agreement of the PSE-3D computations, formulated in a nonorthogonal coordinate system with DNS results, demonstrated that the choice of a suitable coordinate system is essential to analyze the secondary instabilities of stationary crossflow vortices.

2) A comparison of the LST-2D and PSE-3D results, employing θ_{min} as x direction, with DNS, reveals that both stability approaches have an overall good agreement when comparing the shape and location of the perturbation amplitude functions, and this holds for the entire chordwise locations in the linear regime.

3) PSE-3D results align more closely with DNS data due to their ability to include upstream information, thus improving the match over the LST-2D results. This is further evidenced when comparing the n-factor curves, where the LST-2D results significantly underpredict the instability growth. On the other hand, the PSE-3D data exhibits a close agreement with the DNS results, at least in the range of linear growth of the secondary instability, and this holds for both Type I and Type III.

4) The impact of convex surface curvature of the infinite swept wing on the secondary disturbance growth has been analyzed and it turned out that it has a stabilizing impact, resulting in smaller growth rates and, as a consequence, n-factors. This is somehow similar to the impact of surface curvature on the primary crossflow instability.

5) The sensitivity of LST-2D/PSE-3D results to the choice of the out-of-plane (x) direction was addressed considering four different x directions. The findings indicate a marked sensitivity of the LST-2D to the x direction, with significant implications for the computed n-factor, especially when aligned with the inviscid streamline. On the other hand, the nonparallel LST-2D and the parallel PSE-3D display a lower sensitivity to the marching direction compared to the parallel LST-2D behavior. Finally, the PSE-3D results show that for different directions, which slightly deviate from the θ_{min} one, the n-factor curves are almost overlapping, indicating that the *nonlocal* nonparallel approach allows one to retrieve the same integrated growth rate.

6) The latter results highlight the importance of an appropriate choice of the x direction, providing guidelines on the definition of such direction. In particular, the results indicate that in PSE-3D computations a quantitatively good agreement with DNS results is obtained even for small deviations from θ_{min} and including the inviscid streamline direction.

7) The direction θ_{min} is found to be very close to the direction of the crossflow vortex axis and deviates from the direction of the inviscid streamline by an offset of 2–4 deg.

In conclusion, this study contributed to a detailed understanding of the origins of discrepancies found in literature between LST-2D results and DNS in the linear analysis of secondary instabilities of crossflow vortices. Moreover, it demonstrated that the results from the PSE-3D methodology, formulated in a nonorthogonal coordinate system, are in excellent quantitative agreement with DNS results. This methodology could be directly extended to study the nonlinear development of secondary instabilities of stationary crossflow vortices using a plane-marching nonlinear PSE-3D approach.

Appendix: Vectors in a Generalized Nonorthogonal Curvilinear Coordinate System

The stability equations in a nonorthogonal coordinate system have been derived starting from the Navier–Stokes formulated in a generalized nonorthogonal curvilinear coordinate system [53]. When it comes to a nonorthogonal coordinate system a covariant or contravariant formulation of a vector can be adopted. The general meaning of covariance and contravariance refers to how the components of a vector transform under a change of basis. This is represented in Fig. A1, where the covariant and contravariant

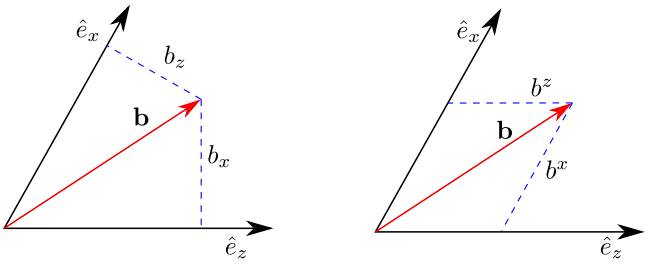

a) Covariant components **b) Contravariant components**

Fig. A1 Sketch of the covariant and contravariant components of a vector when the basis is not orthogonal.

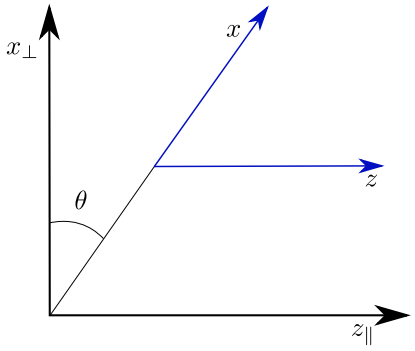

Fig. A2 Coordinate system employed and the relationship between the axes. Reproduced from [25].

components of a generic vector $\boldsymbol{b}$ are portrayed. In particular, the covariant components are perpendicular projections on the base vectors $\hat{e}_x$ and $\hat{e}_z$, whereas its contravariant components are parallel projections. In deriving the equations, a contravariant formulation for the vectors has been employed. Figure A2 and Eq. (12) give information on the coordinate transformations.

$$\begin{aligned} x &= x_\perp / \cos\theta \\ z &= z_\parallel - x_\perp \tan\theta \\ x_\perp &= x\cos\theta \\ z_\parallel &= z + x\sin\theta \end{aligned} \tag{A1}$$

Acknowledgments

This project has received funding from the European Union's Horizon 2020 research and innovation program under the Marie Skłodowska-Curie grant agreement No. 955923. The authors gratefully acknowledge the scientific support and high-performance computing (HPC) resources provided by the German Aerospace Center (DLR). The HPC system CARO is partially funded by the "Ministry of Science and Culture of Lower Saxony" and "Federal Ministry for Economic Affairs and Climate Action".

References

[1] Washburn, A., Campbell, R., Saric, W., Wygnanski, I., Baumann, E., and King, R., "Drag Reduction Status and Plans—Laminar Flow and AFC," *AIAA Aero Sciences Meeting*, AIAA, Reston, VA, 2011.

[2] Sengupta, T. K., and Dipankar, A., "Subcritical Instability on the Attachment-Line of an Infinite Swept Wing," *Journal of Fluid Mechanics*, Vol. 529, 2005, pp. 147–171. https://doi.org/10.1017/S0022112004003246

[3] Li, F., and Choudhari, M. M., "Spatially Developing Secondary Instabilities and Attachment Line Instability in Supersonic Boundary Layers," *46th AIAA Aerospace Sciences Meeting and Exhibit*, AIAA Paper 2008-590, 2008. https://doi.org/10.2514/6.2008-590

[4] Borodulin, V. I., Ivanov, A. V., Kachanov, Y. S., Mischenko, D. A., Örlü, R., Hanifi, A., and Hein, S., "Experimental and Theoretical Study of Swept-Wing Boundary-Layer Instabilities. Three-Dimensional Tollmien-Schlichting Instability," *Physics of Fluids*, Vol. 31, No. 11, 2019, Paper 114104. https://doi.org/10.1063/1.5125812

[5] Saric, W. S., "Görtler Vortices," *Annual Review of Fluid Mechanics*, Vol. 26, No. 1, 1994, pp. 379–409. https://doi.org/10.1146/annurev.fl.26.010194.002115

[6] Dagenhart, J. R., and Saric, W. S., "Crossflow Stability and Transition Experiments in Swept-Wing Flow," NASA Langley Research Center TR XXXX, 1999.

[7] Dallmann, U., and Bieler, H., "Analysis and Simplified Prediction of Primary Instability of Three-Dimensional Boundary-Layer Flows," *AIAA 25th Aerospace Sciences Meeting*, AIAA Paper 1987-1337, 1987. https://doi.org/10.2514/6.1987-1337

[8] Mack, L. M., "Boundary Layer Linear Stability Theory," *Special Course on Stability and Transition of Laminar Flow*, AGARD 709, 1984.

[9] Saric, W., Reed, H., and White, E., "Stability and Transition of Three-Dimensional Boundary Layers," *Annual Review of Fluid Mechanics*, Vol. 35, No. 1, 2003, pp. 413–440. https://doi.org/10.1146/annurev.fluid.35.101101.161045

[10] Bippes, H., "Basic Experiments on Transition in Three-Dimensional Boundary Layers Dominated by Crossflow Instability," *Progress in Aerospace Sciences*, Vol. 35, No. 4, 1999, pp. 363–412. https://doi.org/10.1016/S0376-0421(99)00002-0

[11] Schrader, L.-U., Brandt, L., and Henningson, D. S., "Receptivity Mechanisms in Three-Dimensional Boundary-Layer Flows," *Journal of Fluid Mechanics*, Vol. 618, 2009, pp. 209–241. https://doi.org/10.1017/S0022112008004345

[12] Fischer, T. M., and Dallmann, U., "Primary and Secondary Stability Analysis of a Three-Dimensional Boundary-Layer Flow," *Physics of Fluids*, Vol. 3, No. 10, 1991, pp. 2378–2391. https://doi.org/10.1063/1.858218

[13] Malik, M. R., Li, F., and Chang, C.-L., "Crossflow Disturbances in Three-Dimensional Boundary Layers: Nonlinear Development, Wave Interaction and Secondary Instability," *Journal of Fluid Mechanics*, Vol. 268, 1994, pp. 1–36. https://doi.org/10.1017/S0022112094001242

[14] Wassermann, P., and Kloker, M., "Mechanisms and Passive Control of Crossflow-Vortex-Induced Transition in a Three-Dimensional Boundary Layer," *Journal of Fluid Mechanics*, Vol. 456, 2002, pp. 49–84. https://doi.org/10.1017/S0022112001007418

[15] Koch, W., Bertolotti, F. P., Stolte, A., and Hein, S., "Nonlinear Equilibrium Solutions in a Three-Dimensional Boundary Layer and Their Secondary Instability," *Journal of Fluid Mechanics*, Vol. 406, 2000, pp. 131–174. https://doi.org/10.1017/S0022112099007387

[16] Malik, M. R., Li, F., Choudhari, M. M., and Chang, C.-L., "Secondary Instability of Crossflow Vortices and Swept-Wing Boundary-Layer Transition," *Journal of Fluid Mechanics*, Vol. 399, 1999, pp. 85–115. https://doi.org/10.1017/S0022112099006291

[17] Högberg, M., and Henningson, D., "Secondary Instability of Cross-Flow Vortices in Falkner-Skan-Cooke Boundary Layers," *Journal of Fluid Mechanics*, Vol. 368, 1998, pp. 339–357. https://doi.org/10.1017/S0022112098001931

[18] White, E. B., and Saric, W. S., "Secondary Instability of Crossflow Vortices," *Journal of Fluid Mechanics*, Vol. 525, 1999, pp. 275–308. https://doi.org/10.1017/S002211200400268X

[19] Bonfigli, G., and Kloker, M., "Secondary Instability of Crossflow Vortices: Validation of the Stability Theory by Direct Numerical Simulation," *Journal of Fluid Mechanics*, Vol. 583, 2007, pp. 229–272. https://doi.org/10.1017/S0022112007006179

[20] Li, F., and Choudhari, M. M., "Spatially Developing Secondary Instabilities in Compressible Swept Airfoil Boundary Layers," *Theoretical and Computational Fluid Dynamics*, Vol. 25, Nos. 1–4, 2011, pp. 65–84. https://doi.org/10.1007/s00162-010-0190-x

[21] Xu, G., Chen, J., Liu, G., Dong, S., and Fu, S., "The Secondary Instabilities of Stationary Cross-Flow Vortices in a Mach 6 Swept Wing Flow," *Journal of Fluid Mechanics*, Vol. 873, 2019, pp. 914–941. https://doi.org/10.1017/jfm.2019.397

[22] Groskopf, G., and Kloker, M. J., "Instability and Transition Mechanisms Induced by Skewed Roughness Elements in a High-Speed Laminar Boundary Layer," *Journal of Fluid Mechanics*, Vol. 805, 2016, pp. 262–302. https://doi.org/10.1017/jfm.2016.563

[23] Groot, K., Serpieri, J., Pinna, F., and Kotsonis, M., "Secondary Crossflow Instability Through Global Analysis of Measured Base Flows," *Journal of Fluid Mechanics*, Vol. 846, 2018, pp. 605–653. https://doi.org/10.1017/jfm.2018.253

[24] Groot, K. J., and Eppink, J. L., "Stability Analysis of the Flow over a Swept Forward-Facing Step Using PIV Base Flows," AIAA Paper 2021-0966, 2021. https://doi.org/10.2514/6.2021-0966

[25] Groot, K., and Eppink, J., "Stability Analysis of the Flow over a Swept Forward-Facing Step Using PIV Base Flows in a Nonorthogonal Coordinate System," AIAA Paper 2021-2908, 2021. https://doi.org/10.2514/6.2021-2908

[26] Li, F., Choudhari, M., Paredes, P., and Duan, L., "High-Frequency Instabilities of Stationary Crossflow Vortices in a Hypersonic Boundary Layer," *Physical Review Fluids*, Vol. 1, No. 5, 2016. https://doi.org/10.1103/PhysRevFluids.1.053603

[27] Choudhari, M., Li, F., Paredes, P., and Duan, L., "Evolution of High-Frequency Instabilities in the Presence of Azimuthally Compact Crossflow Vortex Pattern over a Yawed Cone," *Theoretical and Computational Fluid Dynamics*, Vol. 36, No. 2, 2022, pp. 181–204. https://doi.org/10.1007/s00162-021-00594-8

[28] Casacuberta, J., Groot, K., Hickel, S., and Kotsonis, M., "Secondary Instabilities in Swept-Wing Boundary Layers: Direct Numerical Simulations and BiGlobal Stability Analysis," AIAA Paper 2022-2330, 2022. https://doi.org/10.2514/6.2022-2330

[29] Rius-Vidales, A. F., and Kotsonis, M., "Impact of a Forward-Facing Step on the Development of Crossflow Instability," *Journal of Fluid Mechanics*, Vol. 924, No. A34, 2021, pp. 1–14. https://doi.org/10.1017/jfm.2021.497

[30] Serpieri, J., and Kotsonis, M., "Design of a Swept Wing Wind Tunnel Model for Study of Cross-Flow Instability," *33rd American Institute of Aeronautics and Astronautics Applied Aerodynamics Conference*, AIAA Paper 2015-2576, 2015. https://doi.org/10.2514/6.2015-2576

[31] Downs, R. S., and White, E. B., "Free-Stream Turbulence and the Development of Cross-Flow Disturbances," *Journal of Fluid Mechanics*, Vol. 735, 2013, pp. 347–380. https://doi.org/10.1017/jfm.2013.484

[32] Tocci, F., Chauvat, G., Rius-Vidales, A., Kotsonis, M., Hein, S., and Hanifi, A., "Interaction of Crossflow Modes with Forward-Facing Steps: Insights Gained from DNS," *10th IUTAM Symposium on Laminar-Turbulent Transition* (to be published).

[33] Fischer, P., Lottes, J., and Kerkemeier, S., "Nek5000 Web Page," 2008, http://nek5000.mcs.anl.gov.

[34] Bertolotti, F., Herbert, T., and Spalart, P., "Linear and Nonlinear Stability of the Blasius Boundary Layer," *Journal of Fluid Mechanics*, Vol. 242, 1992, pp. 441–474. https://doi.org/10.1017/S0022112092002453

[35] Hosseini, S. M., Vinuesa, R., Schlatter, P., Hanifi, A., and Henningson, D. S., "Direct Numerical Simulation of the Flow Around a Wing Section at Moderate Reynolds Number," *International Journal of Heat and Fluid Flow*, Vol. 61, 2016, pp. 117–128. https://doi.org/10.1016/j.ijheatfluidflow.2016.02.001

[36] Werner, M., Schütte, A., and Weiss, S., "Turbulence Model Effects on Vortex Interaction Prediction on a Multiswept Delta Wing," *Journal of Aircraft*, Vol. 61, No. 1, 2024, pp. 211–221. https://doi.org/10.2514/1.C037421

[37] Banks, D. C., and Singer, B. A., "Vortex Tubes in Turbulent Flows: Identification, Representation, Reconstruction," *Proceedings Visualization '94*, Inst. of Electrical and Electronics Engineers, New York, 1994, pp. 132–139,. https://doi.org/10.1109/VISUAL.1994.346327

[38] Jeong, J., and Hussain, F., "On the Identification of a Vortex," *Journal of Fluid Mechanics*, Vol. 285, 1995, pp. 69–94. https://doi.org/10.1017/S0022112095000462

[39] Theiß, A., Hein, S., Syed Raza, C. A., and Radespiel, R., "Wake Flow Instability Studies Behind Discrete Roughness Elements on a Generic Re-Entry Capsule," *46th American Institute of Aeronautics and Astronautics Fluid Dynamics Conference*, AIAA Paper 2016-4382, 2016. https://doi.org/10.2514/6.2016-4382

[40] Di Giovanni, A., and Stemmer, C., "Cross-Flow-Type Breakdown Induced by Distributed Roughness in the Boundary Layer of a Hypersonic Capsule Configuration," *Journal of Fluid Mechanics*, Vol. 856, 2018, pp. 470–503. https://doi.org/10.1017/jfm.2018.706

[41] Malik, M. R., and Chang, C.-L., "Oblique-Mode Breakdown and Secondary Instability in Supersonic Boundary Layers," *Journal of Fluid Mechanics*, Vol. 273, 1994, pp. 323–360. https://doi.org/10.1017/S0022112094001965

[42] Theiß, A., "Transition Mechanisms on Blunt Re-Entry Capsules With and Without Roughness," Ph.D. Thesis, Technische Universität Braunschweig, Braunschweig, Germany, 2021.

[43] Hernández, J. A., and Hermanns, M., "Stable High-Order Finite-Difference Methods Based on Non-Uniform Grid Point Distributions," *International Journal for Numerical Methods in Fluids*, Vol. 56, No. 3, 2008, pp. 233–255. https://doi.org/10.1002/fld.1510

[44] Malik, M. R., "Numerical Methods for Hypersonic Boundary Layer Stability," *Journal of Computational Physics*, Vol. 86, No. 2, 1990, pp. 376–413. https://doi.org/10.1016/0021-9991(90)90106-B

[45] Welch, P. D., "The use of Fast Fourier Transform for the Estimation of Power Spectra: A Method Based on Time Averaging over Short, Modified Periodograms," *IEEE Transactions on Audio and Electroacoustics*, Vol. 15, No. 2, 1967, pp. 70–73. https://doi.org/10.1109/TAU.1967.1161901

[46] Koch, W., "On the Spatio-Temporal Stability of Primary and Secondary Crossflow Vortices in a Three-Dimensional Boundary Layer," *Journal of Fluid Mechanics*, Vol. 456, 2002, pp. 85–111. https://doi.org/10.1017/S002211200100756X

[47] Gaster, M., "A Note on the Relation Between Temporally-Increasing and Spatially-Increasing Disturbances in Hydrodynamic Stability," *Journal of Fluid Mechanics*, Vol. 14, No. 2, 1962, pp. 222–224. https://doi.org/10.1017/S0022112062001184

[48] Montero, I. P., and Pinna, F., "Analysis of the Instabilities Induced by an Isolated Roughness Element in a Laminar High-Speed Boundary Layer," *Journal of Fluid Mechanics*, Vol. 915, 2021, Paper A90. https://doi.org/10.1017/jfm.2021.70

[49] Li, F., and Malik, M. R., "Fundamental and Subharmonic Secondary Instabilities of Görtler Vortices," *Journal of Fluid Mechanics*, Vol. 297, 1995, pp. 77–100. https://doi.org/10.1017/S0022112095003016

[50] Xu, J., Liu, J., Zhang, Z., and Wu, X., "Spatial-Temporal Transformation for Primary and Secondary Instabilities in Weakly Non-Parallel Shear Flows," *Journal of Fluid Mechanics*, Vol. 959, 2023, Paper A21. https://doi.org/10.1017/jfm.2023.67

[51] Malik, M. R., and Poll, D. I. A., "Effect of Curvature on Cross-Flow Instability," *Laminar-Turbulent Transition*, Springer, Berlin, 1984, pp. 563–571. https://doi.org/10.1007/978-3-642-82462-3_70

[52] Serpieri, J., and Kotsonis, M., "Three-Dimensional Organisation of Primary and Secondary Crossflow Instability," *Journal of Fluid Mechanics*, Vol. 799, 2016, pp. 200–245. https://doi.org/10.1017/jfm.2016.379

[53] Aris, R., "Vectors, Tensors, and the Basic Equations of Fluid Mechanics," *SIAM Review*, Vol. 5, No. 2, 1963, pp. 165–165. https://doi.org/10.1137/1005051

M. Choudhari
Associate Editor